


FULL PAPER

Open Access



Episode 4 (2019–2020) Nishinoshima activity: abrupt transitions in the eruptive style observed by image datasets from multiple satellites

Takayuki Kaneko^{1*} , Fukashi Maeno¹, Mie Ichihara¹, Atsushi Yasuda¹, Takao Ohminato¹, Kenji Nogami², Setsuya Nakada³, Yoshiaki Honda⁴ and Hiroshi Murakami⁵

Abstract

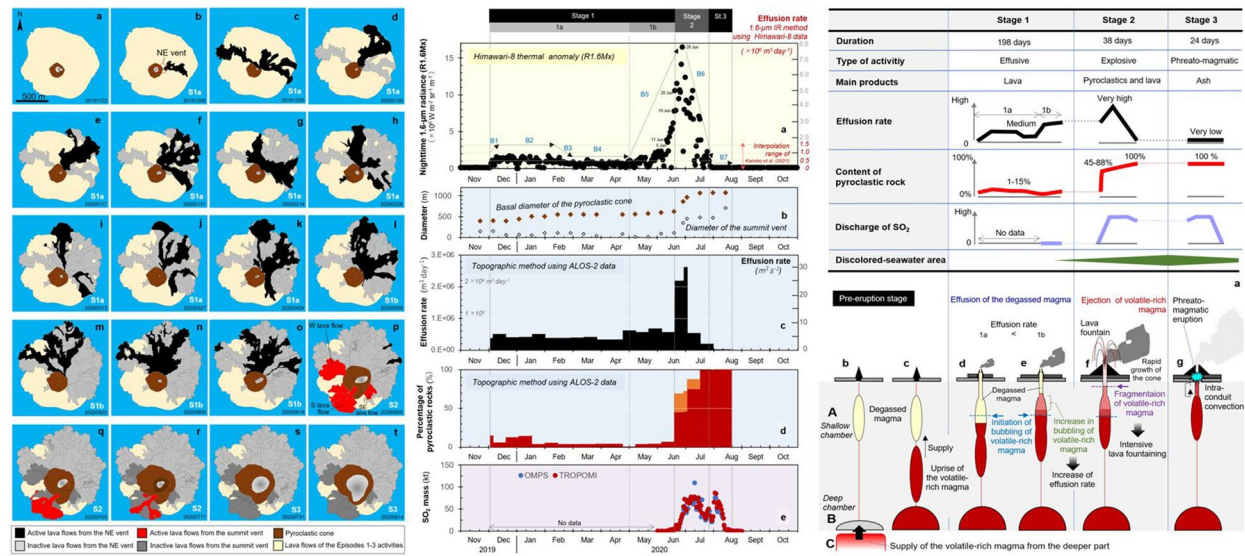
In December 2019, a new activity started at Nishinoshima volcano in the southern part of the Izu–Ogasawara arc, Japan. This is now referred to as Episode 4 of a series of activities that began in 2013. We analyzed the eruption sequence, including erupted volume and effusion rate, based on combined observations of thermal anomalies by Himawari-8 and topographic changes by ALOS-2. The total eruption volume during Episode 4 was $\sim 132 \times 10^6 \text{ m}^3$, and the average effusion rate over the entire period was $0.51 \times 10^6 \text{ m}^3 \text{ day}^{-1}$ ($5.9 \text{ m}^3 \text{ s}^{-1}$), which was two to three times higher than that of Episode 1. Episode 4 had three stages. In Stage 1, effusive activity was dominant, and most of the lava erupted from a northeast vent at the foot of the pyroclastic cone to cover the northern half of the island. The average effusion rate was estimated to be $0.46 \times 10^6 \text{ m}^3 \text{ day}^{-1}$ ($5.3 \text{ m}^3 \text{ s}^{-1}$). In Stage 2, an intensive lava fountain with a high discharge rate developed, and it increased the size of the pyroclastic cone rapidly. The effusion rate temporarily reached $2.6 \times 10^6 \text{ m}^3 \text{ day}^{-1}$ ($30 \text{ m}^3 \text{ s}^{-1}$). Pyroclastic rocks accounted for 45–88% of the total erupted volume in this stage. Lava flows with rafted cone material were generated, and those possibly caused by intensive spatter falls on the slope were also formed. These lavas flowed down the southern half of the island. In Stage 3, continuous phreatomagmatic eruptions released ash and spread it over a wide area. The high effusion rate and the drastic change in the activity style in Episode 4 can be explained by deep volatile-rich magma being supplied to a shallower magma chamber prior to Episode 4. When the volatile-rich magma reached a shallow part of the conduit in Stage 2, fragmentation occurred due to rapid volume expansion to eject large amounts of magma and form the intensive lava fountain. Observations by satellite-borne ultraviolet–visible image sensors detected a rapid increase in SO_2 emissions in response to the intensive lava-fountain activity. The less-differentiated nature of the ash fragments collected during Stage 2 may reflect the composition of the volatile-rich magma. Large-scale discolored-seawater areas appeared during the late period of Stage 1, which may have been caused by ascent of the volatile-rich magma.

*Correspondence: kaneko@eri.u-tokyo.ac.jp

¹ Earthquake Research Institute, The University of Tokyo, 1-1-1 Yayoi, Bunkyo-ku, Tokyo 113-0032, Japan

Full list of author information is available at the end of the article

Graphical Abstract



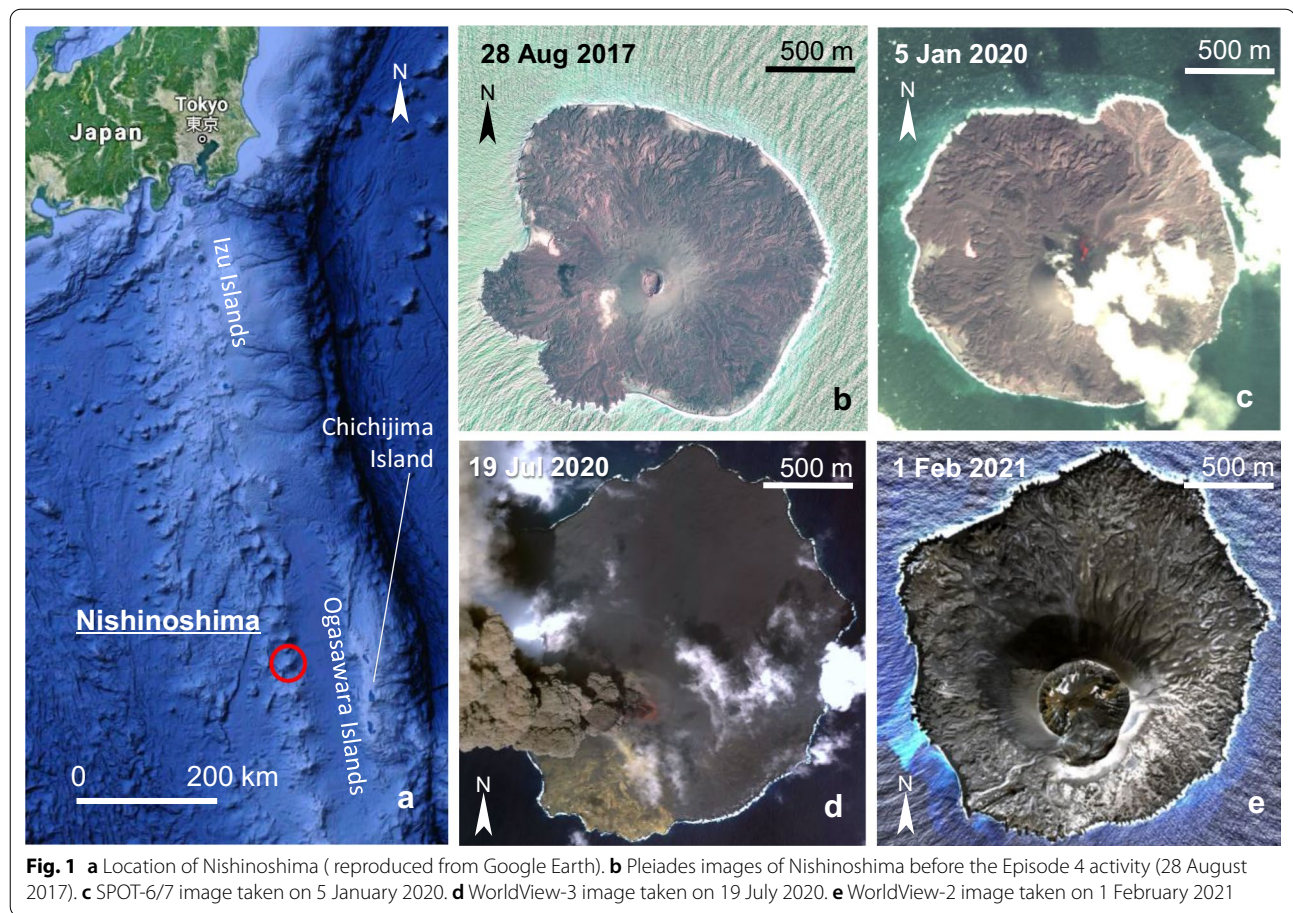
Introduction

In December 2019, a new activity began at Nishinoshima volcano. This is the fourth episode (Episode 4) in a series of eruptive activities that began with Episode 1 in 2013–2015 and was followed by Episode 2 in 2017 and Episode 3 in 2018. During the nine months of Episode 4 activity, although effusive eruptions similar to those in Episodes 1–3 continued for the first seven months, in the late stage, the eruptions changed to very different styles—notably an intensive lava-fountain activity with rapid growth of the pyroclastic cone and then finally release of airfall ash spreading over wide areas. How did the transitions of the eruption mode proceed? What caused these transitions? Answering these questions will lead to understanding not only the Nishinoshima activity, but also the factors that cause abrupt changes in eruption style, which is a key issue in research on eruption sequences.

The area from the Izu Islands to the Mariana Islands via the Ogasawara Islands is called the Izu–Bonin–Mariana arc system, where a number of volcanoes are distributed along the island arcs due to the subduction of the Pacific Plate (Stern et al. 2004). Nishinoshima is in the southern part of the Izu–Ogasawara arc (Fig. 1a). The present Nishinoshima volcano is on the summit of a cone-shaped submarine volcano rising more than 3000 m above the seafloor (Japan Coast Guard 2017). In this location, old lavas, several to tens of several Ka (kilo annum), were exposed on the sea surface (Old Island), and in 1973–1974, the first historical eruptions occurred and formed a small edifice (Umino and Nakano 2007). Although the volcanic island was eroded considerably during the

40 years of dormancy, in November 2013, a new series of activities, which continued until 2020, began at the same site and resumed island-building. In the first activity (Episode 1), effusive eruptions involving Strombolian eruptions continued from November 2013 to December 2015; during that time, the edifice grew into a mature volcanic island with a diameter of about 2 km and a pyroclastic cone about 140 m high in the center (Maeno et al. 2016, 2017, 2018). This was followed by similar effusive activity with Strombolian eruptions in April–August 2017 (Episode 2; Fig. 1b), which grew significantly seaward in the southwestern and western parts of the island (Kaneko et al. 2019b). Further, a small activity occurred in July 2018 (Episode 3), which developed a small-scale lava flow down to the south of the eastern base of the pyroclastic cone (Japan Coast Guard 2021).

The 2019–2020 activity, Episode 4, is inferred to have begun with an initial minor eruption at 21:00 (JST) on 4 December 2019, and then continuous lava effusion started at around 12:00 (JST) on 5 December (Kaneko et al. 2021). On 6 December, the Japan Coast Guard conducted aircraft observations and found that lava was effusing from the northeastern base of the pyroclastic cone and flowing eastward (Japan Coast Guard 2021). In the Episode 4 activity, effusive activity with Strombolian eruptions continued from the beginning of the eruption until mid-June 2020 (Fig. 1c), but from late June to mid-July, an intensive lava-fountain activity occurred and the pyroclastic cone grew rapidly (Yanagisawa et al. 2020). Aerial observations by one of the authors (SN) in late July showed that the activities of lava fountaining and lava



effusion had almost stopped, but ash emission extending over a large area continued, and almost the entire island was covered with airfall-ash deposits (Fig. 1d). Observations on 5 September showed no significant activity, with only a small amount of steam rising from the summit vent of the pyroclastic cone (Japan Coast Guard, 2021; e.g., Fig. 1e).

Nishinoshima is an isolated, inhabited island in the Pacific Ocean, about 1000 km south of Tokyo (Fig. 1a). For this reason, survey and observation methods are limited. Regarding the Episode 4 activity, although more than 10 months have passed since the end of the eruption, land geological surveys have not yet been conducted (as of the end of June 2021). Under these circumstances, we analyzed the eruption sequence and eruption processes of Episode 4 based on the effective combination of satellite images with different characteristics (e.g., Kaneko et al. 2019a; b). We adopted the complementary use of thermal observation using infrared images from Himawari-8, which has high temporal resolution, and topographic observation using synthetic aperture radar (SAR) images from ALOS-2, which is capable of all-weather observation and has high spatial resolution.

Furthermore, for detailed observations of the erupted units, high-resolution optical images (WorldView-2/3, SPOT-6/7) and aerial photographs were analyzed as necessary. Based on these results, here we propose a model to explain the mechanism that caused the characteristic eruption sequence. Further, this model was examined from different viewpoints, such as the temporal variation of SO₂ emissions measured by the Ozone Mapping and Profiler Suite (OMPS) and Tropospheric Monitoring Instrument (TROPOMI) images, the appearance of large-scale areas of discolored seawater observed by the Second-Generation Global Imager (SGLI) onboard the Global Observation Mission-Climate (GCOM-C: SHIKISAI) satellite, and the chemical composition of the ash fragments.

Methods and data

Satellite data

Infrared images obtained by Himawari-8 were used to observe the time-series variation of the thermal anomaly and to estimate the effusion rate. Himawari-8 is a meteorological satellite of the Japan Meteorological Agency (JMA) in geostationary orbit at 140.7°E, about 35,786 km

above the equator (Japan Meteorological Agency 2021). It has 16 bands in wavelengths ranging from 0.47 μm in the visible to 13.3 μm in the thermal infrared, and it can observe the full disk of the earth at 10-min intervals (Japan Meteorological Agency 2021). The resolution for the infrared bands is 2 km. In this study, nighttime images of the 1.6- μm band were used for the analysis. The original Himawari-8 images were downloaded from the National Institute of Information and Communications Technology (NICT) and corrected geometrically and radiometrically. Then, an area of about 200 km \times 200 km with Nishinoshima at the center was cut out. After these were corrected for stray solar light effects (Kaneko et al. 2018b), atmospheric effects (MODTRAN 3.7 subtropical summer/winter models; Berk et al. 1989; atmospheric transmittance at 1.6 μm at an altitude of 100 m was estimated to be 0.89), and emissivity (emissivity at 1.6 μm was assumed to be 0.95 with reference to that in the thermal infrared region; Harris, 2013, Walter and Salisbury 1989), they were used for analysis. The highest value in a 7- \times 7-pixel area containing the Nishinoshima summit at the center (R1.6Mx) was selected from the radiance image, and then the highest R1.6Mx value was chosen from the 50–70 images obtained each night as the thermal anomaly for each day, to minimize the influence from coverage by sub-pixel-sized clouds and eruption plumes. Details of the corrections and data processing for Himawari-8 images are described in Kaneko et al. (2018a, 2019b).

In this study, the topography and distribution of the lava flows, the pyroclastic cone, and airfall-ash deposits were analyzed using high-resolution images, as well as the erupted volume and effusion rate. For frequent observations, we used SAR images from the ALOS-2 satellite as the main data source, as they are hardly affected by clouds and the eruption plume over the volcano. ALOS-2 is a JAXA satellite equipped with an L-band SAR sensor called PALSAR-2 (hereafter simply “ALOS-2 imagery”). The resolution of ALOS-2 images is 3 m \times 1 m in the highest-resolution Spotlight mode (Japan Aerospace Exploration Agency 2021a). ALOS-2 was operated in disaster management mode during the Episode 4 activity of Nishinoshima, and the images were taken at 14-day intervals in Spotlight mode, which made them ideal datasets for observing the eruptive situation on a regular basis. We used 19 Spotlight mode and 1 Stripmap 1 mode (3 m \times 3 m resolution) Level 2.1 images taken between November 2019 and August 2020. High-resolution images from the optical sensor, such as WorldView-2/3 and SPOT-6/7, and published aerial photographs (e.g., Japan Coast Guard 2021) were used to observe details such as the color tone of the erupted units. For WorldView-2/3 and SPOT-6/7 images, pan-sharpened images

were produced from panchromatic- and multi-band images, and then the obtained RGB images were used for interpretation. As a reference for volumetric measurements, we used Digital Elevation Model (DEM) data (grid spacing of 5 m and height in meters) generated from the stereo pairs of WorldView-2 images taken on 1 February 2021.

Methods for estimation of erupted volume and effusion rate

In effusive eruptions, the following two methods are often used for estimation of the discharge rate: one is based on the heat balance of lava flows using infrared images, and the other measures topographic changes using high-resolution images (Harris et al. 2007). Because the infrared-image methods assume effusion-dominant activities, the estimation error might become large if the eruption changes to a non-effusive mode, such as predominant lava fountaining. However, this method can use high-frequency satellite infrared imagery, such as that of Himawari-8, which can provide high-density (i.e., high temporal resolution) estimates of the effusion rate (Kaneko et al. 2021). The topographic method requires high-resolution imagery. Because frequent observations with short intervals are difficult to obtain, the main value obtained here is an average discharge rate for a certain period—a few days to weeks—rather than an instantaneous value. In addition, it is generally necessary to assume the thickness of lava flows, which can be a major source of error. However, the topographic method is not affected by the eruption mode, because it directly measures the topography. In this study, we used both methods in parallel complementarily to obtain more accurate information on the effusion rate and its time-series variation throughout the entire period. Here, we basically use the term “effusion rate” to mean the instantaneous magma discharge rate, and “eruption rate” to describe the average discharge rate over the entire activity period (Wadge 1981), for both lava and pyroclastic rocks. The average discharge rate obtained by the topographic method is consistent with the instantaneous “effusion rate” when the effusion rate remains unchanged for a certain period.

Estimation using infrared images

For estimation using infrared images, we adopted a method based on the 1.6- μm band images of Himawari-8 (Kaneko et al. 2021). In the effusive eruption with low-viscosity lava, a positive correlation was found between the radiance (thermal anomaly) observed in the nighttime 1.6- μm band images from Himawari-8 and effusion rates estimated by the topographic method in the 2015 Raung and the 2017 Nishinoshima activities, and thus by using a regression equation ($Y=0.47 X$) between these

two parameters, the effusion rate ($Y: \times 10^6 \text{ m}^3 \text{ day}^{-1}$) can be estimated from the radiance value ($X: \times 10^6 \text{ W m}^{-2} \text{ sr}^{-1} \text{ m}^{-1}$). Although there are methods to use thermal infrared images (e.g., 11- μm band; Harris et al. 1997, 2007; Harris and Baloga 2009; Wright et al. 2001) and midwave infrared images (e.g., 3.9- μm band; Coppola et al. 2013, 2019), both methods assume a cooling-limited lava flow (Calvari et al. 2003; Guest et al. 1987), which is not appropriate for the activities at Nishinoshima, where contact with seawater is the most influential factor for stopping lava flows (as described below).

Estimation using the topographic method

In the estimation using the topographic method, we conducted the calculation by separating the whole erupted volume into three parts: the pyroclastic cone, lava flows, and airfall ash. Topographic characteristics of the edifice formed in the Episode 4 activity of Nishinoshima are shown in Fig. 2a–d.

Pyroclastic cone The apparent volume of the pyroclastic cone was calculated by approximating it with a truncated cone (e.g., Schmincke 2004), subtracting twice the volume of the small cone (equivalent to the volume above

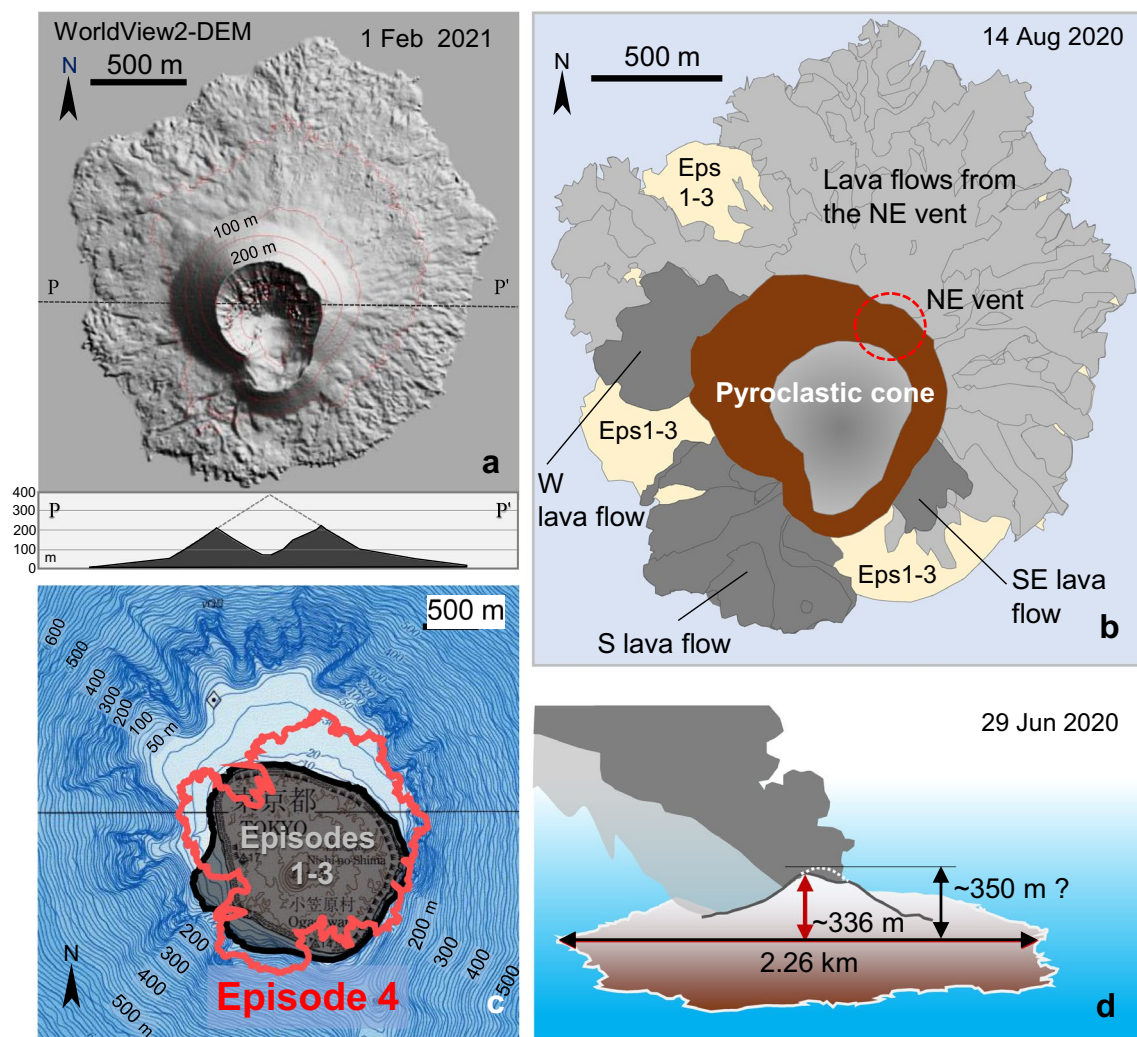


Fig. 2 Topographic characteristics of the edifice formed in the Episode 4 activity of Nishinoshima. **a** Digital Elevation Model (DEM) of Nishinoshima after the Episode 4 activity produced from a stereo pair of WorldView-2 images taken on 1 February 2021 (the same image as Fig. 1e). The lower illustration shows the cross section of the island. **b** Sketch of Nishinoshima in the final stage of the Episode 4 activity. **c** Enlargement of Nishinoshima Island between Episodes 3 and 4 (the base map is a bathymetric chart by the Japan Coast Guard; Japan Coast Guard, 2017). **d** Estimation of the maximum height of Nishinoshima during the Episode 4 activity, based on the aerial photograph taken on 19 June 2020 (Japan Coast Guard 2021)

and inside the summit vent) defined by the summit-vent radius (upper base) from the volume of the large cone calculated using the basal radius (lower base). In both cones, the slope angle was assumed to be 32° (as discussed below). The volume of the pyroclastic rocks composing the pyroclastic cone was converted to a dense rock equivalent (DRE) by assuming the density of lava and pyroclastic rocks to be 2.5 g cm^{-3} and 1.0 g cm^{-3} , respectively (Kaneko et al. 2019b). The effusion rate was calculated by taking the volume difference between the two pyroclastic cones obtained from the two images on adjacent observation days (mostly every 14 days) and dividing this volume by the observation interval. The volume decrease in the pyroclastic cone after the collapse of the inner wall of the summit vent in the terminal stage (31 July–14 August) was excluded from this calculation.

Lava flows The volume of lava flows was determined by multiplying the area of active lava erupted during the observation interval by the average thickness of the active lava (which usually consisted of several overlapping lava flows). The effusion rate was calculated by dividing the obtained value by the observation interval. The average thickness of the active lava was determined (7.2 m for the 14-day interval), so that the apparent total volume of the onshore part of the volcano (including Episodes 1–3; e.g., Geospatial Information Authority of Japan 2018) at the end of the activity (14 August) matched the relevant volume of the DEM produced from the WorldView-2 stereo images taken on 1 February 2021 (Fig. 2a) to minimize the systematic errors in the volume estimates. The volume of lava beneath the sea surface was estimated using the topographic map of the seafloor published by the Japan Coast Guard (2017) (Fig. 2c).

Airfall ash Because the depositional situation of airfall ash was unknown, this study assumed that, during the period in which the pyroclastic cone was growing (mainly Stages 1 and 2, described below), 20% of the total volume of pyroclastic rocks was emitted as airfall ash (i.e., 80% landed on the pyroclastic cone). In the late period of Episode 4, when the growth of the pyroclastic cone had stopped (mainly Stage 3, described below), the emission volume of airfall ash was assumed to be 50% of that during the period 17–31 July. For the calculation of the erupted volume and effusion rate, the DRE value was used, as in the case of the pyroclastic cone.

Results

The activity in Episode 4 can be divided into three stages (Fig. 3): Stage 1 (4 December 2019–19 June 2020), Stage 2 (20 June–27 July 2020), and Stage 3 (28 July–20 August 2020), as described in the last part of this section. Time-series variations of the parameters relating to the eruptive

situation during the Episode 4 activity of Nishinoshima are shown in Fig. 3a–e.

Time-series variations of thermal anomaly observed by Himawari-8

Using the nighttime $1.6\text{-}\mu\text{m}$ images from Himawari-8, we examined the time-series variations of thermal anomalies (R1.6Mx) during the Episode 4 activity (Fig. 3a). The whole activity period was divided into seven blocks using the points at which the radiance trend changed. After the start of lava effusion on 5 December 2019, the thermal anomaly slowly rose (B1 in Stage 1a) from the background level and remained almost constant at around $1.3 \times 10^6 \text{ W m}^{-2} \text{ sr}^{-1} \text{ m}^{-1}$ for two months (B2 in Stage 1a). At the end of February 2020, it showed a downward trend (B3 in Stage 1a). The thermal anomaly remained relatively low at around $0.5 \times 10^6 \text{ W m}^{-2} \text{ sr}^{-1} \text{ m}^{-1}$ during March and April (B4 in Stage 1a), but began to increase from the beginning of May, accelerated in June, and reached an unprecedentedly high value, $16.5 \times 10^6 \text{ W m}^{-2} \text{ sr}^{-1} \text{ m}^{-1}$, in late June (B5 in Stages 1b–2). The thermal anomaly peaked on 28 June and then rapidly decreased (B6 in Stages 2–3), reaching the background level by the end of July. After that, no thermal anomaly was observed (B7 in Stage 3).

Geological interpretation of the eruptive activities based on the ALOS-2 images

The results of a geological interpretation of the eruption sequence for the Episode 4 activity based on the ALOS-2 images are shown in Fig. 4a–t. High-resolution satellite images and aerial photographs of the Episode 4 activity are shown in Fig. 5a–m. In the following, we describe the results in terms of the three main components of the Episode 4 activity: lava flows, the pyroclastic cone, and airfall ash.

Lava flows

The lava flows during Episode 4 can be divided into two groups: those generated by the effusive activity involving the Strombolian eruptions from December 2019 to mid-June 2020 (Stage 1), and those associated with the intensive lava-fountain activity from late June to mid-July 2020 (Stage 2).

Lava flows generated by the effusive activity with Strombolian eruptions Most of the lava flows associated with the effusive activity were effused from the vent at the north-eastern base of the pyroclastic cone (hereafter referred to as the “NE vent”, although the topographic shape of the NE vent itself is not clear; Figs. 2b, 4b, 5b). Another vent was present in the same period on the southwestern slope of the pyroclastic cone, where a small lava flow effused (Fig. 4h).

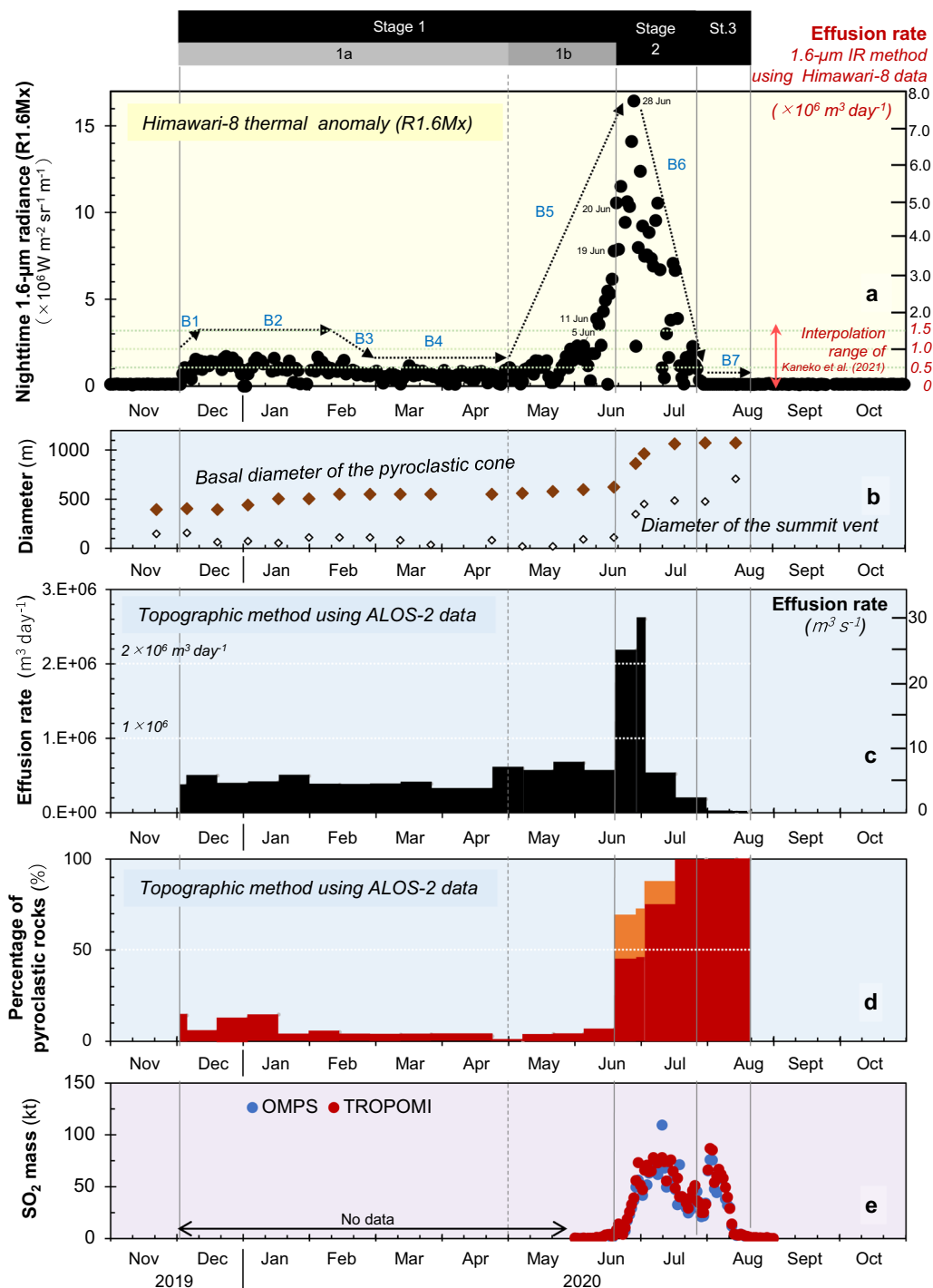


Fig. 3 Time-series variations of the parameters relating to the eruptive situation during the Episode 4 activity of Nishinoshima. **a** Time-series variation of the nighttime 1.6-μm radiance observed by Himawari-8 (R1.6Mx). The estimated effusion rate based on the 1.6-μm IR method (Kaneko et al. 2021) is shown on the right side. **b** Time-series variation of the basal diameter of the pyroclastic cone and diameter of the summit vent based on the ALOS-2 images. **c** Time-series variation of the effusion rate estimated by the topographic method using the ALOS-2 images. **d** Time-series variation of the content percentage of pyroclastic rocks in the erupted volume. The upper ends of the orange columns show estimations that assume 50% of the volume of the Stage 2 lava flows to have a pyroclastic origin. **e** Time-series variation of SO_2 mass in the Western Pacific area based on the ultraviolet–visible satellite observation (OMPS and TROPOMI) by the NASA Goddard Space Flight Center (NASA Goddard Space Flight Center 2021)



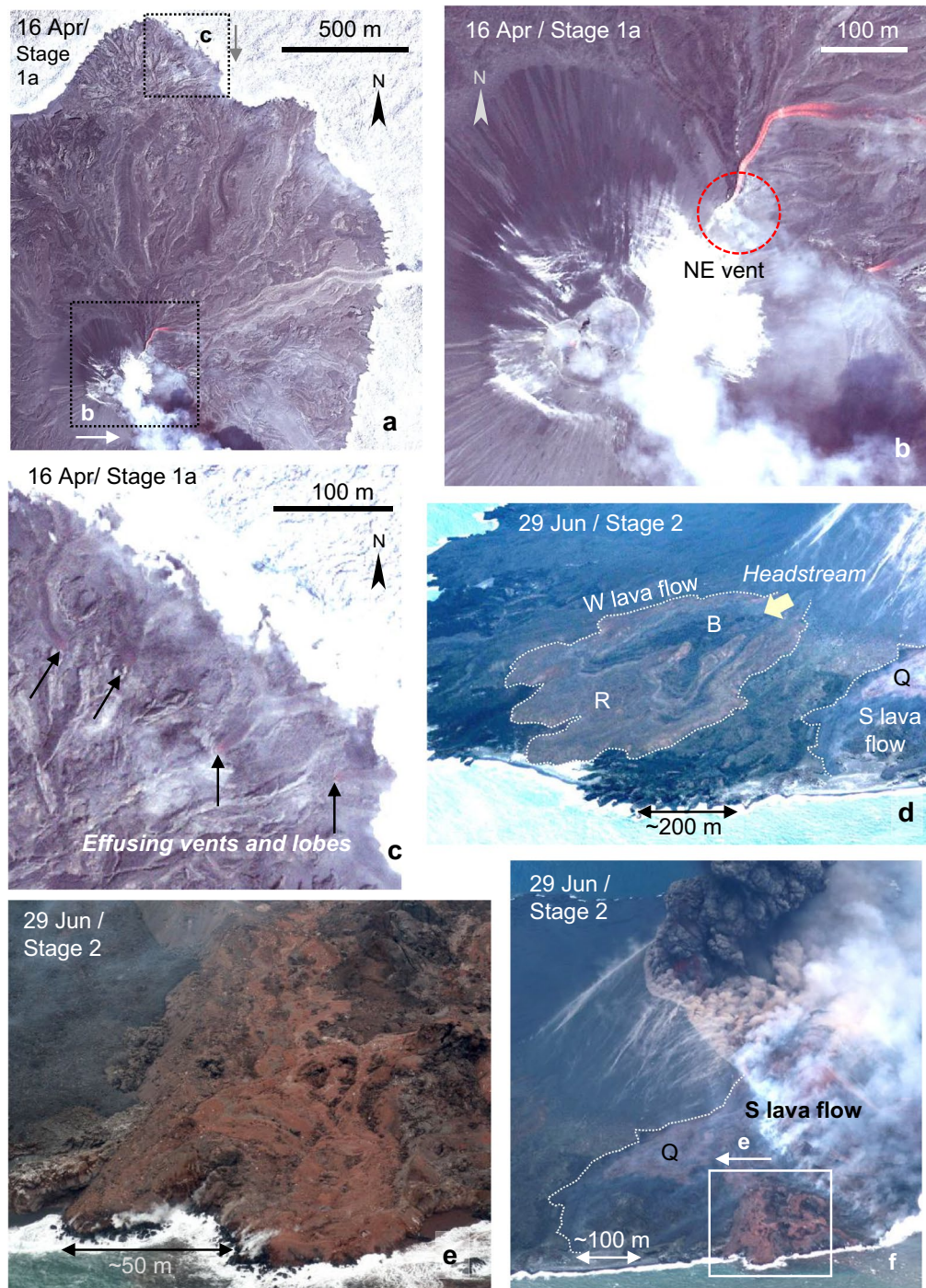


Fig. 5 High-resolution satellite images and aerial photographs of the Episode 4 activity of Nishinoshima. **a** Northeastern part of Nishinoshima taken on 16 April 2020 (WorldView-3). **b** Close-up of the northeastern part of the pyroclastic cone (the same image as **a**). **c** Close-up of part of the deltaic landform near the coast formed by small lava lobes (the same image as **a**). **d** Aerial photograph of the Western lava flow taken on 29 June by the Japan Coast Guard (Japan Coast Guard 2021); “Q” is the same point as in **f**. **e** Close-up of the flow front of the Southern lava flow taken on 29 June by the Japan Coast Guard (Japan Coast Guard 2021). **f** Southwestern slope of the pyroclastic cone photographed on 29 June by the Japan Coast Guard (Japan Coast Guard 2021). **g** Main part of the Southern lava flow and the pyroclastic cone imaged on 3 July 2020 (ALOS-2). **h** The same area as **g** and **i** on 17 July 2020 (ALOS-2). **i** The same area as **g** and **h** on 31 July 2020 (ALOS-2). **j** Flow front of the Southern lava flow imaged on 19 July (WorldView-3). Many large blocks can be recognized on the surface. **k** Lava fountain observed from a JMA observation vessel on 11 July (imaged by JMA). **l** Release of fine ash resulting from the phreatomagmatic eruption (imaged on 30 July by SN). **m** Wide-spread ash plume released by the phreatomagmatic eruptions of Stage 3 observed by Himawari-8 on 2 August 2020 (NICT Science Cloud 2021)

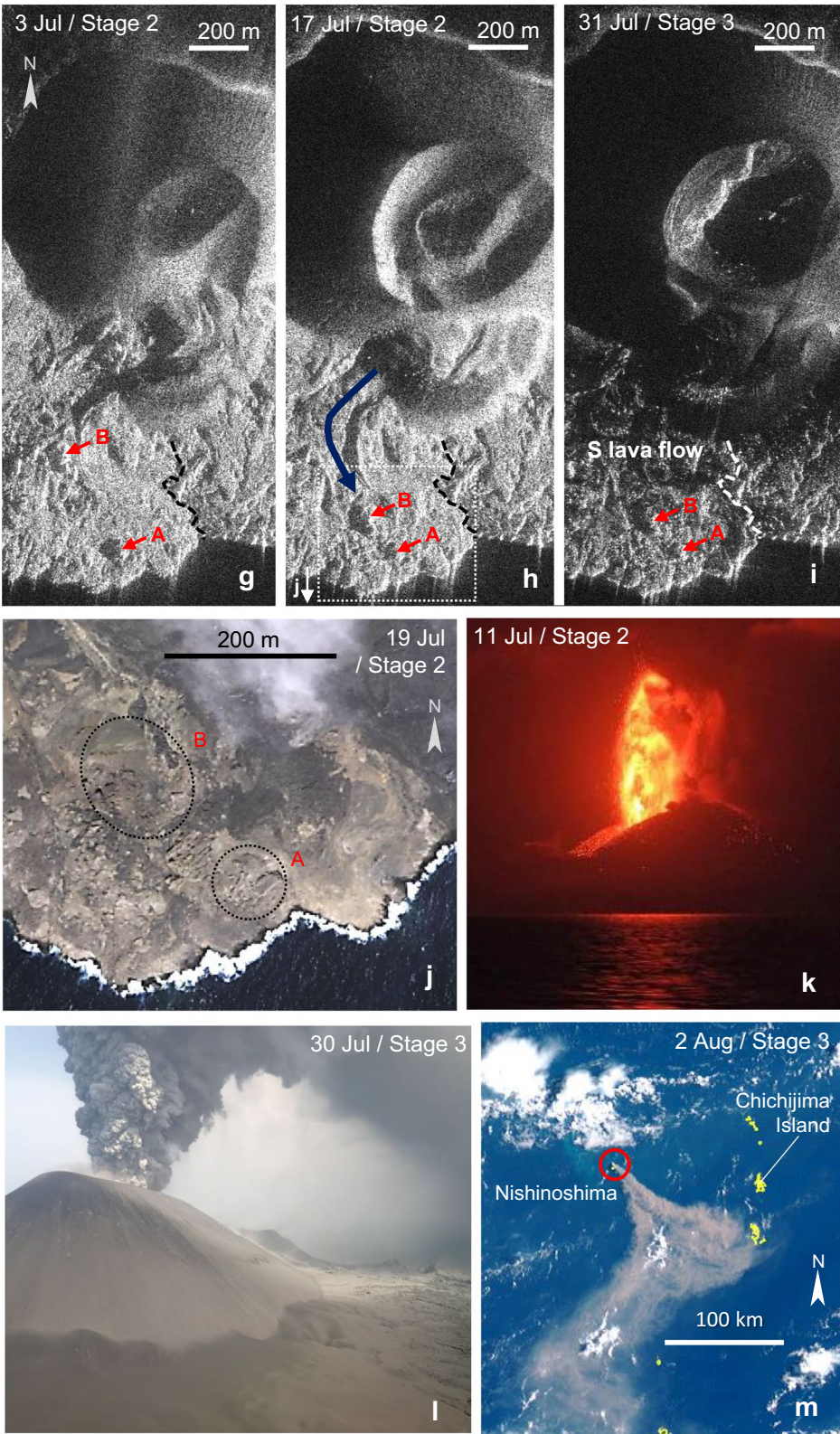


Fig. 5 continued

Lava flows effused from the NE vent

Lava effused continuously from the NE vent for about seven months from the beginning of Episode 4, and eventually covered the northern half of the island (Fig. 4b–o). These were all dark-colored and low-viscosity lava flows—the distribution was well-controlled by the topography, and small elongated tributaries were formed. From this vent, simultaneous flows in two directions were commonly observed. Lava was also transported downstream from the vicinity of the NE vent through lava tubes and effused at the foot of the slope (e.g., Fig. 4h, m). The lava flows from the NE vent were wide compared to those during Episodes 1–3, and many of them reached the coast almost without branching. In Episodes 1–3, lava flows often branched in a dendritic manner shortly after effusion from the vent (upper left parts of Fig. 1b, c), but when the effusion rate was high, the lava flows became long and wide (Kaneko et al. 2019b; Maeno et al. 2016). The topographic features of the lava flows from the NE vent in Episode 4 may reflect the continuously high lava effusion rate.

Small lava flow from the southwestern slope of the pyroclastic cone

Between 14 and 28 February, a small lava flow effused from the middle of the southwestern slope of the pyroclastic cone and flowed downward toward the southwest (Fig. 4h). This lava flow occurred episodically, and no continuous lava effusion was observed here. Similar small-scale lava flows had occurred on the southern slopes of the pyroclastic cone in Episodes 1 and 2 (Kaneko et al. 2019b; Maeno et al. 2018).

Lava flows accompanied by intensive lava fountains Lava flows formed in association with intensive lava fountaining (e.g., Fig. 5k; Stage 2) are distributed on the western, southern, and south-eastern sides of the island. They are divided into three flows according to the distribution. All the lava flows were formed after 19 June, and peak of the activity was between 20 and 29 June. Unlike the lava flows from the NE vent, many of these have complex surface structures, including reddish lava and collapsed blocks from a part of the pyroclastic cone.

Western lava flow

The Western lava flow fans out westward from the pyroclastic cone (W lava flow in Fig. 4p) and consists of red lava at the lower part (R in Fig. 5d) and black lava at the upper part (B in Fig. 5d). There is a possibility that the red lava is clastogenic lava formed by the rapid deposition of oxidized magma fragments ejected by the intensive lava fountain (Sumner 1998) on the steep slope of the cone, as observed in the 1983 Puu Oo episode 9 activity,

Kilauea, Hawaii (Wolfe et al. 1988). The black lava also can be clastogenic lava from the low fountain or effused lava from the summit vent or breaches on the slope. It has a smooth surface and is not accompanied by large blocks on the surface. From the distribution, the source is estimated to be in the direction of the summit of the pyroclastic cone (arrow in Fig. 5d), but no topographic traces are found on the slope. Because the Western lava flow was formed during the rapid growth of the pyroclastic cone, the upstream area was probably covered by later ejecta.

Southern lava flow

Topographically, the Southern lava flow appears to have been formed by the deposits spreading to the south resulting from the U-shaped collapse of the southern part of the pyroclastic cone including the summit (S lava flow in Figs. 4p, 5g–i). It has well-developed levees and looks thicker than the flows from the NE vent. Based on the ALOS-2 images, the outline of the Southern lava flow was formed between 20 and 29 June (Yanagisawa et al. 2020), and by 19 July several subsequent units had flowed and settled above the previous ones. Numerous large blocks are found on the surface, which are considered to be rafted material derived from the partial collapse of the pyroclastic cone due to lava effusion from within (Fig. 5j; Wolfe et al. 1988). In fact, the surface mega-blocks are recognized to have moved downstream along the lava flow (blocks “A” and “B” in Fig. 5g–i). Red lava, found mainly in the lower part (Fig. 5e, f), might be formed by intense spatter falls on the slope (Wolfe et al. 1988), prior to the partial collapse of the cone summit, possibly at the same phase as the occurrence of the red lava of the Western lava flow. The Southern lava flow is a complex lava flow composed of reddish lava flows (possibly clastogenic) constituting the lower parts, and the overlying lava flow with rafted cone material effused from the interior of the pyroclastic cone. In the northwestern part of the Southern lava flow, no rafted cone material can be seen.

Southeastern lava flow

The Southeastern lava flow is located at the south-eastern foot of the island (SE lava flow in Fig. 4p) and is short but wide at the bottom of the pyroclastic cone. The Southeastern lava flow is considered not to be accompanied by rafted cone material, as in the case of the Western and the northwestern part of the Southern lava flows, because the surface looks flat with few undulations.

Enlargement of the distribution area of lava flows As in Episodes 1–3, the area of the island became significantly enlarged during Episode 4 due to the continuous inflow of lava into the sea. Figure 2c shows the enlargement of

the island between Episodes 3 and 4. Especially, the northern side of the island was enlarged greatly because the NE vent was located on this side and the seabed was shallow. The topography of the seabed had a great influence on the current shape of Nishinoshima.

Repeated effusion of vast numbers of lava flows forms a lava flow field (Kilburn 2000) around the pyroclastic cone. In the Nishinoshima activities, many tiny lobes effused from the breaches in the solidified flow front of the lava flows that had reached the coastal areas (Maeno et al. 2016), and often formed deltaic landforms (Fig. 5a, c). This may be related to the forced cooling by seawater and subsequent cessation of lava flow. As to the mechanism for stopping the movement of lava flows, cooling-limited and volume-limited types have been proposed (Calvari et al. 2003; Guest et al. 1987); however, at Nishinoshima, unlike these types, the main cause was basically “forced suspension due to external factors—contact with seawater”. This is largely related to the fact that Nishinoshima is a newly formed volcanic island in the ocean. This also affected the lava flow topography, such as formation of deltaic landforms with small lobes on the coastal areas.

Pyroclastic cone

Elevation change and slope angle The height of the pyroclastic cone, which is the highest point on Nishinoshima, was 160 m just before the Episode 4 activity began (Geospatial Information Authority of Japan 2021), but it increased to about 250 m by the end of Episode 4 (WorldView2-DEM; Fig. 2a). However, it was much higher than 250 m during the most active period of lava fountaining (Stage 2), and the maximum height was estimated to have reached about 330–340 m above sea level on 29 June based on the analysis of aerial photographs (Fig. 2d). This summit’s height is considered to have been diminished by partial collapses (Yanagisawa et al. 2020), giving an expected maximum height of around 350 m.

Regarding the slope angle of the pyroclastic cone, it was 32° just before the start of Episode 4 (Geospatial Information Authority of Japan 2021) and 32° on 14 August 2020, in the final period of Episode 4 (WorldView2-DEM), as well. This value is consistent with the slope angle of scoria cones, as determined by the angle of repose (McGetchin et al. 1974) of 32°–33° (Schmincke 2004), suggesting that the pyroclastic cone on Nishinoshima had grown by rock fragments ejected by the lava fountain, forming a slope with the angle of repose.

Changes in the basal diameter and the summit-vent diameter Figure 3b shows the time-series variation in the basal diameter and summit-vent diameter of the pyroclastic cone. During the period of effusive activities, from

December 2019 to mid-June 2020 (Stage 1), the basal diameter increased slightly with time, becoming enlarged from 395 to 624 m in 6.5 months, which is about 1.5 times larger than the initial size. In contrast, the stage of the intensive lava-fountain activity, from the end of June to mid-July (Stage 2), was marked by rapid growth of the pyroclastic cone, where the basal diameter doubled from 624 m to 1065 m within one month. After this, there was little growth of the pyroclastic cone. The diameter of the summit vent of the pyroclastic cone fluctuated between 18 and 147 m during the effusive stage, but increased rapidly in the intensive lava-fountain stage, reaching 707 m at the end of Stage 3, which is larger than the basal diameter of the pyroclastic cone before Episode 4. This is the largest class of pyroclastic cone vent diameter (usually 50–600 m; Schmincke 2004). The rapid increase in the summit-vent diameter may have been caused by the intensive lava-fountain activity, which became more explosive than that in the effusive stage (Stage 1). After 17 July, the summit-vent diameter and depth had increased mainly due to the collapse of the inner wall of the vent (Figs. 4r–t, 5h–i), including a double crater rim formed in late Stage 2 (Fig. 5h; Yanagisawa et al. 2020).

Airfall ash

In Episode 4, the activity became more explosive toward the end, and thus generation of ash became more prominent. From December 2019 to mid-June 2020 (Stage 1), during the effusive stage of lava flows from the NE vent, the generation of ash was limited. In this period, the eruption plume was whitish-grey from the beginning until the end of May, and it darkened slightly in June (Japan Coast Guard 2021). The deposition of airfall ash (mainly scoria) on the island became more pronounced after the transition to the intensive lava-fountain activity, accompanied by a dense ash-rich eruption plume in late June (Stage 2; Figs. 1d, 5f). Initially, airfall ash covered the northeastern part of the island and this area became enlarged to the northern half of the island by mid-July (Fig. 4p–s). Although the growth of the pyroclastic cone almost stopped by mid-July, the release of ash continued beyond this time, and ultimately the entire island was covered with airfall ash (Fig. 5l; Stage 3), making it impossible to identify the microtopography of the lava flows. The eruption plume in this stage was whitish-gray and widely dispersed over a distance more than several 100 km from the summit crater (Fig. 5m), suggesting a release of fine ash due to high explosivity. Moreover, the inner wall of the summit vent collapsed during this period (Fig. 5h–i). Intense generation of fine ash and the summit collapse suggest that the magma head was lower than the top of the aquifer at this time, inducing phreatomagmatic eruptions that produced fine-grained ash

particles. Ash emission declined in mid-August and was almost absent by the end of this month. In the Episode 1–3 activities of Nishinoshima, the effusion rate gradually decreased, and at the same time, the Strombolian (occasionally Vulcanian) eruptions became more sporadic, after which the activity eventually ceased. Phreatomagmatic eruptions did not occur in the late stage of the activity in these cases.

Time-series variations of effusion rate, erupted volume and the ratio of lava and pyroclastic rocks in the erupted volume during Episode 4

The effusion rate estimated by the method using the nighttime 1.6- μm band images of Himawari-8 (hereafter “1.6- μm IR method”) is shown on the right side of Fig. 3a. This method cannot be applied to the activity since late June 2020 (Stage 2) because effusion of lava was not the main activity mode; thus, the values of effusion rate during this period may not be adequate quantitatively. Figure 3c and Table 1 show the variation of the effusion rate estimated topographically based on the ALOS-2 imagery (hereafter “topographic method”).

Both methods show good agreement in terms of the pattern of time-series variations for the entire period, and absolute values during the period from December 2019

to the end of May 2020 (Stage 1), while the effusive activity was dominant (Fig. 3a, c). From December 2019 to April 2020, the effusion rates were $0.4\text{--}0.8 \times 10^6 \text{ m}^3 \text{ day}^{-1}$ ($4.6\text{--}9.3 \text{ m}^3 \text{ s}^{-1}$) for the 1.6- μm IR method and $0.3\text{--}0.6 \times 10^6 \text{ m}^3 \text{ day}^{-1}$ ($3.5\text{--}6.9 \text{ m}^3 \text{ s}^{-1}$) for the topographic method. From the beginning of May (Stage 1b), both methods show the effusion rates starting to increase. In mid-June, although the effusion rate estimated by the topographic method remained at the same level as that in May (Fig. 3c), the thermal anomaly started to increase sharply (Fig. 3a), probably due to a slight increase in Strombolian activity, as suggested by the dark plume. From late June to the beginning of July (Stage 2), when the activity of the lava fountain was at its peak, the maximum value was $2.6 \times 10^6 \text{ m}^3 \text{ day}^{-1}$ ($30 \text{ m}^3 \text{ s}^{-1}$) according to the topographic method (this value is the average of 4 days, so the effusion rate may have been higher than this). The effusion obtained by the 1.6- μm IR method also peaked at this time, but the absolute value was systematically higher ($7.7 \times 10^6 \text{ m}^3 \text{ day}^{-1}$: $89 \text{ m}^3 \text{ s}^{-1}$). This is considered to reflect the fact that magma was released as lava fountaining (which is probably more thermally radiative per unit of magma discharge compared with lava effusion), and the effusion rate was an instantaneous value. After that, the effusion rate decreased rapidly, according

Table 1 Effusion rate, cumulative erupted volume, and content of pyroclastic rocks estimated by the topographic method using ALOS-2 images

Episode 4/stage	Date	Term (day)	Effusion rate		Cumulative erupted volume (m^3)	Content percentage of pyroclastic rocks (%)
			($\text{m}^3 \text{ day}^{-1}$)	($\text{m}^3 \text{ s}^{-1}$)		
Stage 1	5 Dec 2019–6 Dec 2019	1	380,000	4.40	428,000	14
	7 Dec 2019–20 Dec 2019	14	501,000	5.80	7,570,000	6
	21 Dec 2019–3 Jan 2020	14	389,000	4.50	13,100,000	13
	4 Jan 2020–17 Jan 2020	14	415,000	4.80	18,900,000	15
	18 Jan 2020–31 Jan 2020	14	496,000	5.74	26,100,000	3
	1 Feb 2020–14 Feb 2020	14	379,000	4.38	31,500,000	5
	15 Feb 2020–28 Feb 2020	14	371,000	4.29	36,900,000	2
	1 Mar 2020–13 Mar 2020	14	379,000	4.39	42,300,000	4
	14 Mar 2020–27 Mar 2020	14	390,000	4.52	47,900,000	4
	28 Mar 2020–24 Apr 2020	28	319,000	3.69	57,100,000	3
	25 Apr 2020–8 May 2020	14	598,000	6.92	65,700,000	1
	9 May 2020–22 May 2020	14	563,000	6.52	73,800,000	4
	23 May 2020–5 Jun 2020	14	670,000	7.75	83,400,000	4
	6 Jun 2020–19 Jun 2020	14	559,000	6.46	91,400,000	7
	20 Jun 2020–29 Jun 2020	10	2,190,000	25.30	113,000,000	45 (69*)
Stage 2	30 Jun 2020–3 Jul 2020	4	2,610,000	30.20	123,000,000	45 (73*)
	4 Jul 2020–17 Jul 2020	14	523,000	6.06	130,000,000	75 (88*)
	18 Jul 2020–31 Jul 2020	14	187,000	2.16	132,000,000	100
Stage 3	1 Aug 2020–14 Aug 2020	14	8210	0.10	132,000,000	100
	15 Aug 2020–20 Aug 2020	6	16,400	0.19	132,000,000	100

The values with asterisks in parentheses in the last column show the results when 50% of the Stage 2 lava is assumed to be derived from the lava-fountain activity

to both methods, and was almost zero by the end of July. The total eruption volume of Episode 4 was $132 \times 10^6 \text{ m}^3$, and the average effusion rate over the entire period (eruption rate) was $0.51 \times 10^6 \text{ m}^3 \text{ day}^{-1}$ ($5.9 \text{ m}^3 \text{ s}^{-1}$).

We distinguished between lava and pyroclastic rocks in the erupted volume to examine the eruptive situation. Figure 3d shows the time-series variation of the ratio of lava (lava flows) and pyroclastic rocks (the pyroclastic cone and airfall ash converted to DRE). In Stage 2, because the lava flows potentially contain both effused lava and clastogenic lava derived from the lava fountain, estimations that assume 50% of their volume to have pyroclastic origin are also shown by using the upper ends of the orange columns in Fig. 3d. This chart shows that pyroclastic rocks accounted for about 1–15% of the volume during the effusive activity, but 45–88% of the volume during the intensive lava-fountain activity. During the intensive lava-fountain activity, the effusion rate increased rapidly, to more than five times that in the effusive stage (Fig. 3c), and at the same time half or more of the volume was ejected as pyroclastic rocks (Fig. 3d).

Comparison of eruption rate, eruption volume, and activity period of Episode 4 and Episodes 1–3

The eruption volume, eruption rate, and duration of the Episode 4 and Episode 1–3 activities are summarized in Fig. 6 based on the existing data (Japan Coast Guard 2021; Kaneko et al. 2019b; Maeno et al. 2016, 2017, 2018) and our estimates. At Nishinoshima, the eruption rate, eruption volume, and activity period decreased gradually from Episode 1 to Episode 3. However, the activity of

Episode 4 started with a high effusion rate, two to three times higher than the eruption rate of Episode 1, and reached a value more than 10 times higher at its peak. The total eruption volume of Episode 4 is almost the same as that of Episode 1. In this way, in the series of activities at Nishinoshima since 2013, Episode 4 is a significant departure from the diminishing trend seen from Episode 1 to Episode 3.

Eruption sequence of Episode 4

The activity of Episode 4 can be divided into three stages based on the differences in the dominant modes of eruptions as described below. Stage 1 (4 December 2019–19 June 2020) was mainly effusive activity, Stage 2 (20 June–27 July 2020) featured intensive lava-fountain activity and rapid growth of the pyroclastic cone, and Stage 3 (28 July–20 August 2020) was characterized by continuous phreatomagmatic eruptions and release of fine ash. Note that the above dates include ambiguities of a few days because of the difficulty in dividing the stages into a range of days. The outline and characteristics of each stage are described below and summarized in Fig. 7a.

Stage 1: period of effusive activity

Stage 1 occupies 76% (198 days) of all 260 days of the Episode 4 activity. The average effusion rate was about $0.46 \times 10^6 \text{ m}^3 \text{ day}^{-1}$ ($5.3 \text{ m}^3 \text{ s}^{-1}$), which was more than two to three times higher than the eruption rate of Episode 1 ($0.2 \times 10^6 \text{ m}^3 \text{ day}^{-1}$; $2.3 \text{ m}^3 \text{ s}^{-1}$; Maeno et al. 2016). The change in the effusion rate in this stage was gradual,

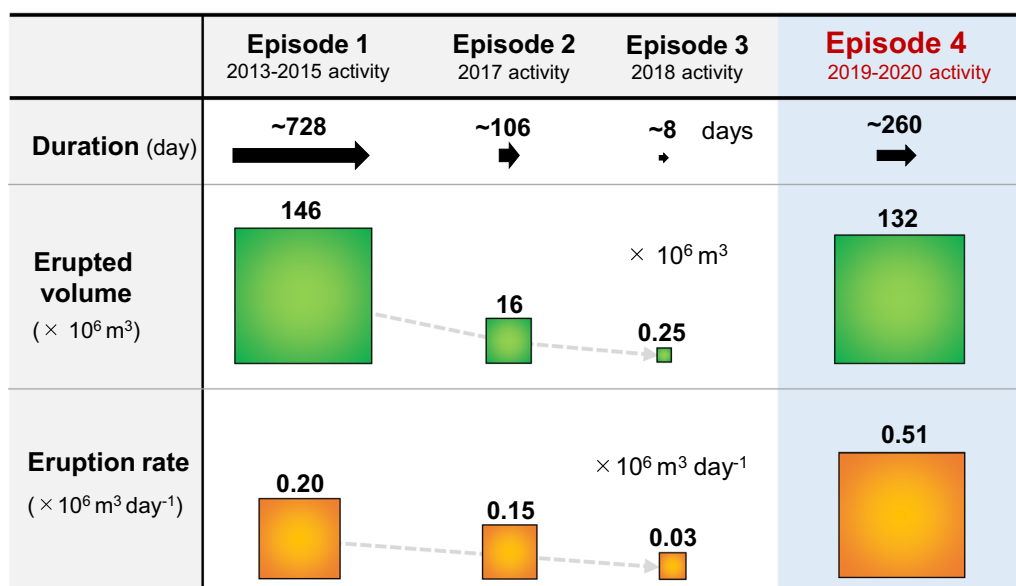


Fig. 6 Comparison of activity period, erupted volume and eruption rate for Episode 4 and Episodes 1–3

	Stage 1	Stage 2	Stage 3
Duration	198 days	38 days	24 days
Type of activity	Effusive	Explosive	Phreato-magmatic
Main products	Lava	Pyroclastics and lava	Ash
Effusion rate			
Content of pyroclastic rock			
Discharge of SO₂			
Discolored-seawater area			

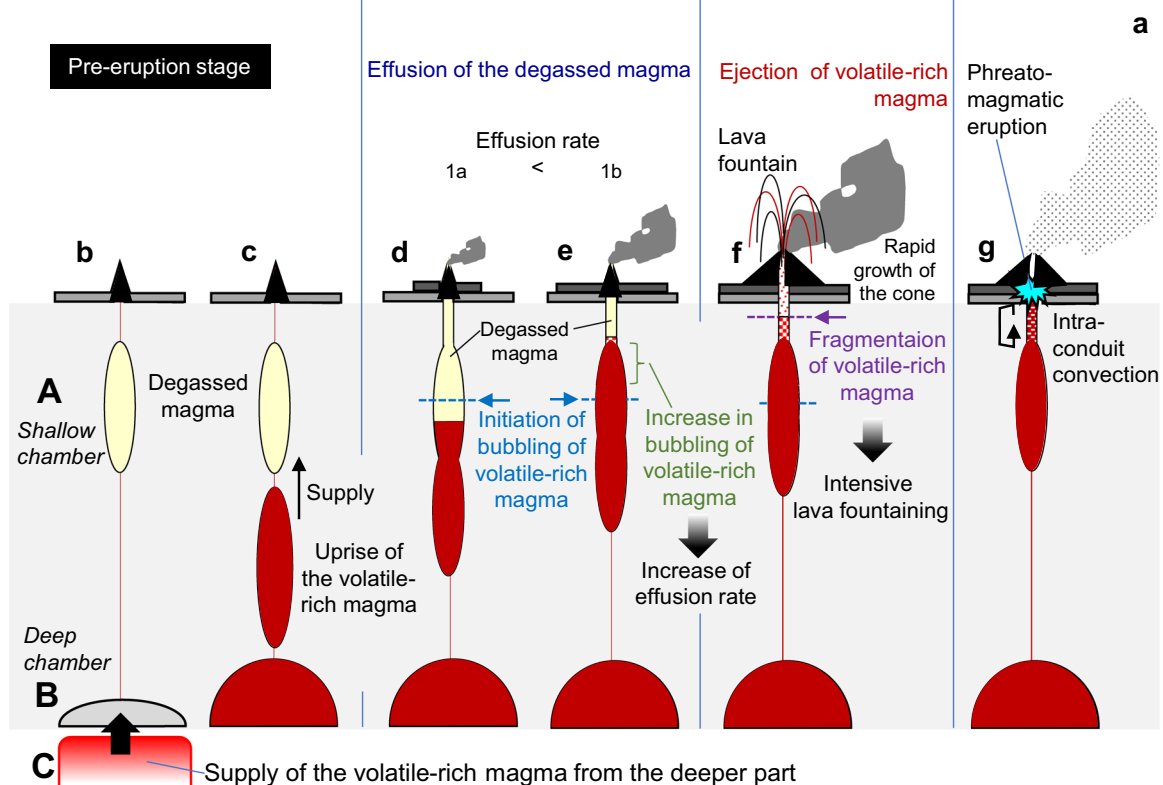


Fig. 7 a Summary of the eruption sequence of the Episode 4 activity of Nishinoshima. **b–g** Possible model to explain the high effusion rate and abrupt transitions in the eruption modes of Episode 4

and the range of the variation was small except in June (Fig. 3a, c). The effusion rate decreased slightly from March to April, and then started to increase from the beginning of May (this is the boundary between Stages 1a and 1b; Fig. 3a, upper part). This upward trend in effusion rates continued after mid-May, leading to an accelerated increase in Stage 2. In Stage 1, most of the lava effused from the NE vent. Stage 1 was basically similar to Episodes 1–3 in terms of the prevalence of effusive activity—pyroclastic rocks accounted for about 1–15% of the erupted volume. However, the high effusion rate resulted in a topographic difference in the prevalence of long, broad lava flows. The Strombolian eruptions on the pyroclastic cone continued, which gradually increased the size of the edifice. Release of ash was limited, and no noticeable ash deposition was observed on the lava flows from the satellite imagery. In June, the eruption plume darkened slightly, suggesting a slight increase in Strombolian activity.

The end of Stage 1 is defined as 19 June, when the last effusive activity was observed in an ALOS-2 image (Fig. 4o).

Stage 2: period of intensive lava-fountain activity

Stage 2 occurred over a short time, 15% (38 days) of the total active period. The effusion rate peaked on 28 June ($2.6 \times 10^6 \text{ m}^3 \text{ day}^{-1}$; $30 \text{ m}^3 \text{ s}^{-1}$; Fig. 3a, c); the peak was five times higher than the eruption rate of Episode 4 ($0.51 \times 10^6 \text{ m}^3 \text{ day}^{-1}$; $5.9 \text{ m}^3 \text{ s}^{-1}$). After this, the effusion rate dropped sharply and was estimated to have reached a very low level by late July (Fig. 3a, c). In Stage 2, intensive lava-fountain activity occurred prevalently with a high effusion rate, and pyroclastic rocks accounted about 45–88% of the erupted volume (Fig. 3d), which made the pyroclastic cone grow rapidly. Related to the lava-fountain activity, ash (mainly scoria) was generated and covered wide areas of the Stage 1 lava flows. Due to an increase in the explosive intensity, the diameter of the summit vent of the pyroclastic cone enlarged rapidly. The pyroclastic cone grew with its slope forming an angle of repose, and the elevation is thought to have reached a maximum of about 350 m.

In Stage 2, unusual lava flows were generated relating to the intensive lava-fountain activity and partial collapse of the pyroclastic cone. The reddish color of the lower units of the Western and Southern lava flows suggests that they might be clastogenic lava flows caused by the dense accumulation of oxidized agglutinates generated by the intensive lava fountain. Furthermore, the Southern lava flow carried vast numbers of fragments of the pyroclastic cone that had partially collapsed due to lava effusion. No lava effusion was observed from the NE vent during this period (the NE vent itself was buried in the pyroclastic cone), except for some effusion via lava tubes on 29 June 2020 (Fig. 4p).

It is difficult to determine the end of Stage 2, but in this paper, the end of Stage 2 is defined as 27 July, just before the radiance of the thermal anomaly dropped to the background level (Fig. 3a).

Stage 3: period of continuous phreatomagmatic eruptions

In Stage 3, there was almost no growth of the pyroclastic cone, and only fine ash was released due to the continuous phreatomagmatic eruptions, and the effusion rate was low. The inner wall of the summit vent of the pyroclastic crater collapsed and the vent gradually became enlarged (Fig. 5h–i).

The end of Stage 3 was set as 20 August, when no significant release of ash was observed (this coincides with the time when the amount of SO_2 derived from Nishinoshima fell below 1 kt, as described below).

Discussion

The points that might be related to the generation mechanism of the characteristic Episode 4 activity can be summarized as follows:

- (1) The eruption rate was two to three times higher than that of Episode 1. Among the series of Nishinoshima activities since 2013, Episode 4 deviated significantly from the overall trend of diminishing activity from Episode 1 to Episode 3, which implies the possibility that another new series of activity had begun.
- (2) In contrast to the previous Episode 1–3 activities, the eruption style changed drastically from effusive to intensive lava fountaining to finally phreatomagmatic eruptions. This suggests that a different mechanism than that of Episodes 1–3 may have been involved in the Episode 4 activity.
- (3) The rapid increase in the effusion rate and the shift to the intensive lava-fountain activity between Stages 1 and 2 occurred together, which suggests that these had the same cause.

In the following discussion, we compare the eruption sequence and time-series variations of the effusion rate and effused volume of Episode 4 with those of Episodes 1–3, using existing magma models for the past activities in Nishinoshima to investigate how items (1) to (3) (listed above) occurred in Episode 4.

Magma model of Nishinoshima volcano

The above-mentioned characteristics in Episode 4 are phenomena closely related to the magma system of Nishinoshima volcano. Here, we examine existing

magma models developed for the Nishinoshima Episode 1–3 activities (Maeno et al. 2018).

In the previous studies, the magma system at Nishinoshima was thought to be as follows: (i) the magma system consists of two magma chambers, a small shallow chamber (A) consisting of slightly differentiated magma ($\text{SiO}_2 \sim 60$ wt%), and a deep large chamber (B) consisting of less-differentiated magma ($\text{SiO}_2 < 60$ wt%) (Fig. 7b). (ii) Magma rises from deep magma chamber (B) and mixes with the magma in shallow chamber (A) to form erupted magma.

The effused lava became slightly depleted in SiO_2 from Episode 1 to Episode 3 (< 1 wt% of SiO_2), which was presumed to be due to a gradual increase in the proportion of mixing from deep magma chamber (B) (Maeno et al. 2018).

Proposed model for Episode 4 activity

Considering the above model, the systematic change in the volumetric parameters in Episodes 1–3 (Fig. 6) shows that the magma repeatedly rose from deep magma chamber (B) according to each episode, and the size of the rising magma batch became gradually smaller in each episode. This may be due to a decrease in the amount of magma left in deep magma chamber (B) by the amount released by the ascent to shallow chamber (A). (The conduit between magma chambers A and B had been warmed by repeated magma ascent since 2013, allowing even small batches of magma to ascend.)

According to this model, the increase in the erupted volume and eruption rate (and effusion rate) in Episode 4 is interpreted as an increase in the size of the magma batch rising from deep magma chamber (B) to shallow magma chamber (A). Here, we consider the possibility that volatile-rich magma was supplied from a much deeper part (C) to deep magma chamber (B) before the beginning of Episode 4. Based on this hypothesis, we examine how we can explain the transitions in the activity style during Episode 4.

Before stage 1

From the deeper part (C), volatile-rich magma was supplied to deep magma chamber (B) (Fig. 7b). In response to this magma supply, a large magma batch was supplied from deep magma chamber (B) to shallow chamber (A) (Fig. 7c).

Stage 1: effusive activity with higher effusion rate

Stage 1 activity began with the eruption of magma from shallow magma chamber (A) to the surface (Fig. 7d). The magma effusion rate was higher than those in Episodes

1–3 because shallow magma chamber (A) had already received a large magma supply. However, the magma erupting to the surface was degassed magma in Stage 1 (the magma was likely to have been a slightly differentiated magma of the same series as those of Episodes 1–3 ($\text{SiO}_2 \sim 60$ wt%) that had remained in shallow magma chamber (A) since the end of Episode 3). For this reason, activity was dominated by lava effusion, as in the Episode 1–3 activities.

In May, the effusion rate began to increase gradually (Stage 1b). This may have been caused by an increase in buoyancy and volume expansion due to decompression foaming as the volatile-rich magma had reached the shallow part of the conduit (Fig. 7e). In contrast, the erupted magma itself continued to be poor in volatile content. In the late period of Stage 1b (June), an increase in Strombolian activity is suggested by the observations that the eruption plume, which had been whitish-grey since the beginning, became dark (rich in ash) (Japan Coast Guard 2021). This might have been caused by the volatiles released from the volatile-rich magma, which were partially entrained into the overlying degassed magma.

Stage 2: intensive lava fountaining and ejection of volatile-rich magma

The rapid transition from Stage 1 to 2 can be considered to have occurred when most of the degassed magma had been released and the volatile-rich magma had reached the fragmentation depth in the conduit. Expansion of the volatile-rich magma in the conduit prompted effective ejection of fragmented magma, which led to formation of the intensive lava fountain and highly efficient magma ejection (Fig. 7f). As a result, it became explosive, and the effusion rate increased sharply at the same time. The production of airfall ash (mainly scoria at this stage) also increased rapidly. The rapid decrease in the effusion rate in the latter half of Stage 2 is thought to be due to exhaustion of magma in the shallow part of the conduit by ejection.

In Stage 2, no lava eruption occurred from the NE vent. The magma that erupted from the NE vent is considered to have moved laterally from the conduit, branching from the magma ejected through the central vent of the pyroclastic cone. Based on numerical simulations, it is estimated that an effusion rate larger than 10^5 kg s^{-1} prohibits gas segregation and lateral magma transport, creating explosive eruptions from the central vent of a pyroclastic cone (Pioli et al. 2008). The average effusion rate in Stage 2 was $0.6 \sim 0.8 \times 10^5 \text{ kg s}^{-1}$, which was close to this critical value; thus, the lateral magma transport might have been stopped, resulting in the termination of lava effusion from the NE vent.

Stage 3: continuous phreatomagmatic eruption

Due to the release of a large amount of magma in Stage 2, in Stage 3 the magma head fell below the upper surface of the aquifer, so that seawater flowed into the conduit and encountered the magma, causing continuous phreatomagmatic eruptions (Fig. 7g). These explosions produced fine-grained ash, which formed an eruption plume and spread widely over an area extending more than 100 km from the island.

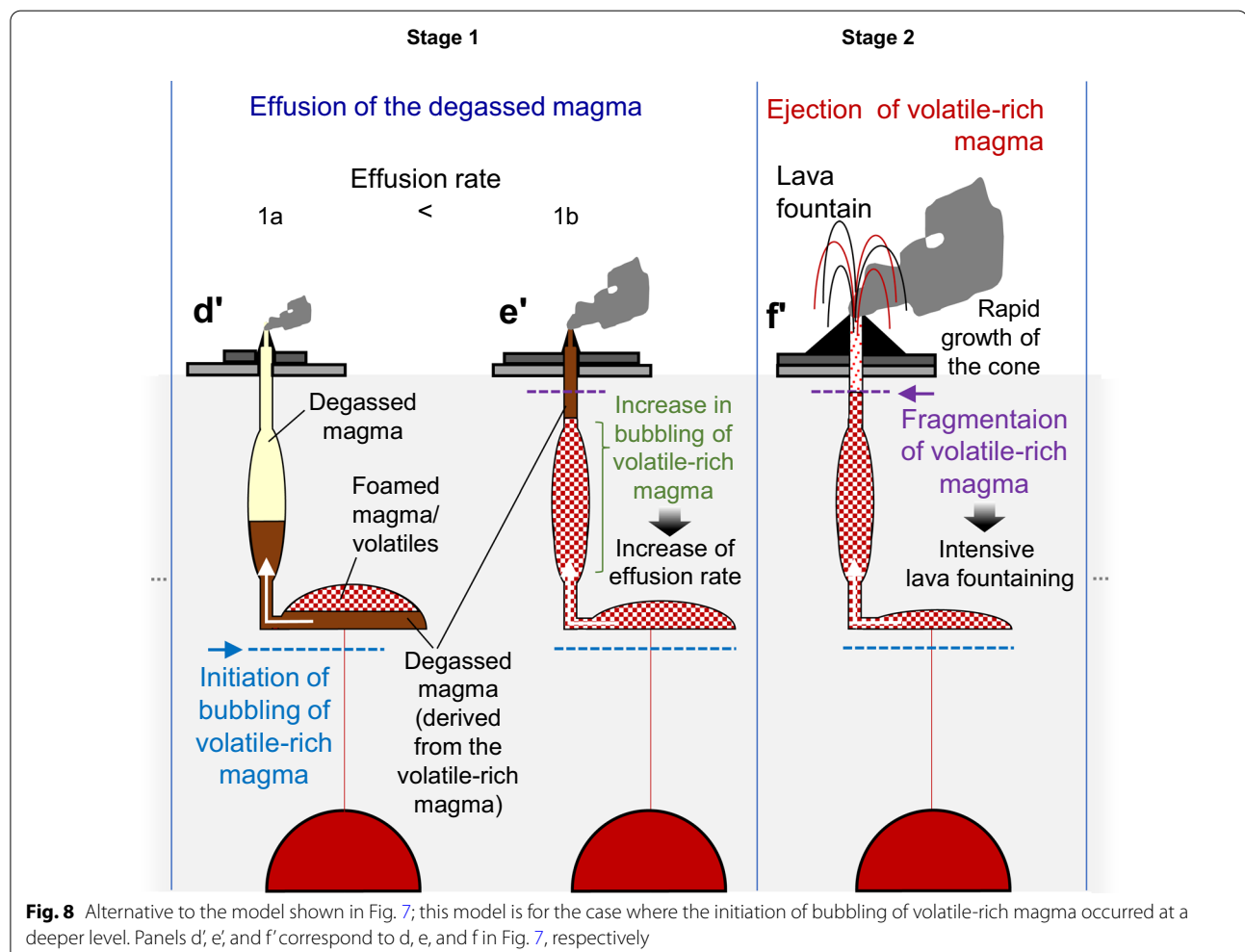
Alternative model

The above model assumes that degassing started at a relatively shallow depth (Fig. 7d, e, which shows the initiation of bubbling of volatile-rich magma). However, there is a possibility that it occurred at a deeper level. In such a case, in the model shown in Fig. 7, the activity is expected to be intensive from the early period because exsolved volatiles were supplied from the volatile-rich magma from the beginning of Stage 1. However, the explosive activity occurred only at the late stage of the activity

(Stage 2), after the prolonged effusive activity (Stage 1). Even if degassing occurred at a deeper level, the observed activity can be explained by assuming that the volatile-rich magma supplied from deep magma chamber (B) formed a lenticular magma chamber (sill) having a connection to magma chamber (A) at its lower part (Fig. 8). In this model, a foamed magma/volatile mixture accumulated in the upper region of the lenticular magma chamber, and degassed magma filled the middle to the lower regions. Initially, the degassed magma was supplied to the magma chamber (A) through the connection to cause the effusive activity during Stage 1. Once the majority of the degassed magma was discharged, foamed magma/volatiles were supplied to the magma chamber (A), which caused the explosive activity in Stage 2.

Supply of volatile-rich magma and transition of eruption styles

We hypothesize that the transition from effusive to explosive eruptions was caused by the ascent of the



volatile-rich magma supplied from the deeper part to the shallow part of the conduit. The viscosity of Nishinoshima's lavas, having basaltic andesite to andesite compositions, is thought to be similar to that of basalts, because of their high temperature (for the Episode 1 lavas having 59–60 wt% SiO₂, the temperature and viscosity were estimated to be 1,050 °C and 10⁴–10⁶ Pa s, respectively; Maeno et al. 2016, 2017, 2018). However, even low-viscosity magmas like basalts can undergo explosive eruptions, including Plinian to sub-Plinian eruptions, after fragmentation (e.g., Houghton and Gonnermann 2008).

Volatiles are considered to be one of the factors influencing the eruption style (Gonnermann and Manga 2012; Houghton and Gonnermann 2008; Pyle and Pyle 1995; Woods and Cardoso 1997). When magma ascends to shallower depths, decompression causes volatile exsolution and bubble growth due to the decrease in solubility of the volatiles in the magma (Gonnermann and Manga 2007; Houghton and Gonnermann 2008; Sparks 1978). Ascent of magma leads to a volume expansion of the exsolved volatiles due to decompression (Sparks 1978). Therefore, when magma and bubbles ascend as a closed system, the decompression also leads to rapid bubble growth and build-up of overpressure, which eventually causes magma fragmentation (Alidibirov and Dingwell 1996; Gonnermann and Manga 2007) and explosive eruptions. In the case of volatile-depleted magma, the potential for explosive eruption decreases. The transition in the eruptive style during Episode 4 of Nishinoshima may reflect these differences. Also in Kilauea, Hawaii, explosive eruptions have been noted in association with a supply of more undifferentiated and volatile-rich magmas from greater depths (Sides et al. 2014).

According to Yanagisawa et al. (2020), the height of the lava fountain during Stage 2 of Nishinoshima Episode 4 was about 200 m (Fig. 5k), which is considered equivalent to a violent Strombolian eruption (Macdonald, 1972; Pioli et al. 2008). The Stage 2 eruption did not evolve to a Plinian or sub-Plinian mode, probably because the viscosity of the magma was not high enough to cause such highly explosive eruptions (La Spina et al. 2021). The viscosity of the Stage 2 magma would be lower than that in Episode 1, as inferred from the lower SiO₂ content of the ash fragments (described below). Although Strombolian and Hawaiian eruptions show various transitions in the eruption style within these categories during an activity (Houghton and Gonnermann, 2008), the Episode 4 activity of Nishinoshima is characterized by a complete transition in the eruption style from effusion dominant to lava-fountain dominant.

Related phenomena

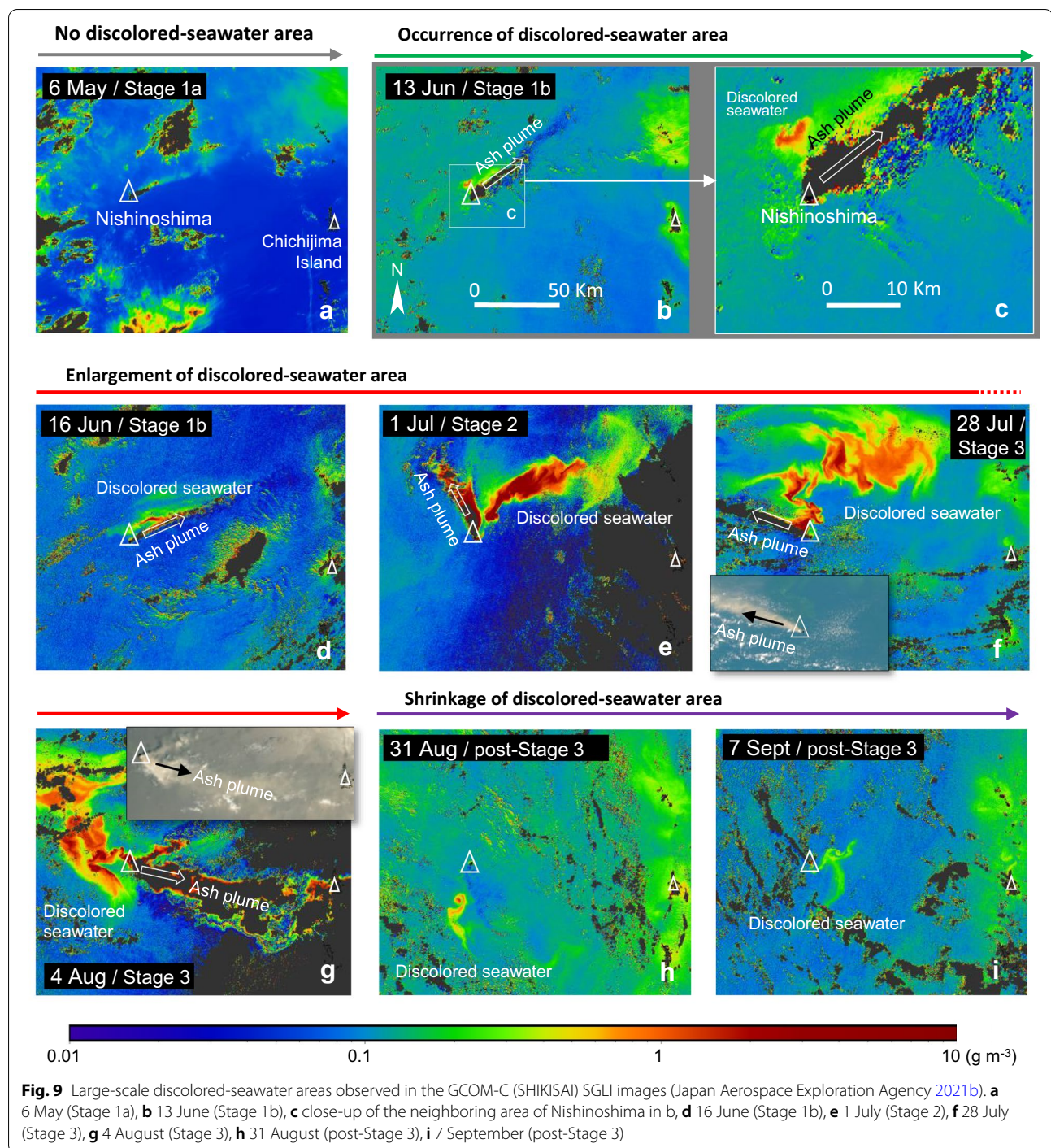
SO₂ emissions

A rapid increase in SO₂ emission was observed simultaneously with the possible eruption of volatile-rich magma in Stage 2. Figure 3e shows the temporal variation of SO₂ in the Western Pacific region, including Nishinoshima, observed by the satellite-borne ultraviolet–visible sensors OMPS and TROPOMI (NASA Goddard Space Flight Center 2021). SO₂ emissions are almost absent from the beginning of Stage 1 until May, but large SO₂ emissions from Nishinoshima were observed in synchronization with the intensive lava-fountain activity and the rapid increase in the effusion rate in late June. The start of this mass release of SO₂ strongly confirms that the magma changed to a volatile-rich composition at the same time as the eruption mode changed. At its peak, it is estimated that tens of thousands of tons of SO₂ released from Nishinoshima were present in the atmosphere in this area (Fig. 3e; Nishinoshima was the only major source of SO₂ emissions in the Western Pacific region during this period). Using the OMPS image of 3 July, the SO₂ emission rate was roughly estimated to be about 10–20 kt day^{−1}, based on the SO₂ concentration of the plume around 300 km northeast of Nishinoshima in the image (4 DU, 200 km width) and the assumed wind speed (5–10 m s^{−1}).

However, the high level of SO₂ emissions continued even in Stage 3, when the magma discharge was drastically reduced. This indicates that SO₂ was transported from the deep to the shallow parts by magma convection in the conduit (Kazahaya et al. 2004). This is similar to the SO₂ mass release stage associated with the phreatomagmatic eruptions just after caldera formation in the 2000 Miyakejima eruption (Kazahaya et al. 2004). This process may have led to the degassing and solidification of magma in the shallow part of the magma supply system, which eventually led to the cessation of activity.

Chemical composition of ash fragments of stage 2

On 11 July 2020, during Stage 2, the intensive lava-fountain activity (Fig. 5k) ejected ash fragments onto a JMA observation vessel navigating near Nishinoshima. We made preliminary analysis of the chemical composition. The results show that the ash fragments of Stage 2 were 54–55 wt% SiO₂ and 3.9–4.0 wt% MgO, which represents a less silica-rich and more MgO-rich composition—undifferentiated magma—than the makeup of all the materials recently erupted from Nishinoshima, including during Episodes 1–3. This undifferentiated magma might be the magma supplied from deeper part (C) in our model (Fig. 7b), and it might have contained a certain amount of volatile components, which may have led to the high SO₂ emissions and high explosivity in Stage



2. The magma erupted during Stage 1 is considered to be the residual magma of Episodes 1–3 ($\text{SiO}_2 \sim 60$ wt%) as described above, but we cannot rule out the possibility that a part of it is the degassed part of the magma supplied from the deeper part (SiO_2 : 54–55 wt%; e.g., the alternative model: Fig. 8). At present, the full extent of the petrological characteristics of the Episode 4 activity is

not known, and it is necessary to confirm them through future investigations on the island.

Occurrence of large-scale discolored-seawater areas

During Episode 4 of the Nishinoshima eruptions, the transition from effusive activity in Stage 1 to the intensive lava-fountain activity in Stage 2 was synchronized with

the occurrence of large-scale discolored-seawater areas. Near-real-time observation of total suspended matter (TSM) concentrations in the sea was carried out using SGLI images from the GCOM-C (SHIKISAI) satellite by JAXA (Japan Aerospace Exploration Agency 2021b). The TSM is the weight density of suspended particles, which includes organic particles (e.g., phytoplankton particles) and inorganic particles (e.g., soil particles, having sufficient size to produce turbidity, but not small molecules that dissolve like ions). The TSM concentration in seawater was estimated using the 490-nm and 565-nm images of the SGLI (Toratani 2021). Because the seas around Nishinoshima are subtropical and oligotrophic, we can assume that the TSM represents the weight density of inorganic particles (due to volcanic activity). Based on these observations, we examined the extent and evolution of discolored-seawater areas in the Izu–Ogasawara Sea area, which includes Nishinoshima (Fig. 9). No discolored seawater was observed from the beginning until the late period of Stage 1. The first large-scale discolored-seawater area was observed on 13 June (Fig. 9b, c), which roughly coincides with the timing of a rapid increase in the effusion rate and possible ascent of the volatile-rich magma to a shallow depth in the conduit. After that, large-scale discolored-seawater areas were observed continuously (Fig. 9d–g) until mid-August. Shortly after the surface eruptive activity had ceased, the discolored-seawater areas began to shrink significantly and disappeared by the beginning of September (Fig. 9h, i).

The discolored-seawater areas are thought to be caused by formation of very fine $\text{SiO}_2\text{-Fe}_2\text{O}_3\text{-Al}_2\text{O}_3\text{-H}_2\text{O}$ low-crystalline precipitates resulting from mixing and neutralizing between the seawater and acidic hydrothermal fluids released from the seabed during volcanic activity (Ossaka et al. 2000). Such discolored seawater is thought to have been distributed only on the surface of the ocean. The inflow of lava into the sea can also cause discolored seawater, but this is likely to be on a local scale—in fact there was no significant discolored-seawater area in Stage 1 despite lava actively flowing into the sea. Although air-fall ash falling into the sea may also have discolored the seawater, the direction and extent of the eruption plume do not match the distribution area of the discolored seawater (Fig. 9e–g). Therefore, in this activity, it is possible that the discolored seawater was generated by the mixing of the hydrothermal water released from the subaqueous parts of the edifice with the seawater by the mechanism presented by Ossaka et al. (2000). The initiation of degassing associated with the ascent of volatile-rich magma to shallow depths in mid- to late-June is thought to have facilitated production of hydrothermal fluids within the edifice, leading to the formation of large-scale areas of discolored seawater.

Conclusions

We analyzed the eruption sequence based on satellite images for the Episode 4 activity that occurred in Nishinoshima from December 2019 to August 2020. The results obtained here can be summarized as follows:

1. The activity of Episode 4 can be divided into three stages based on the differences in the dominant eruption modes: Stage 1—mainly effusive activity; Stage 2—intensive lava-fountain activity and rapid growth of the pyroclastic cone; and Stage 3—continuous phreatomagmatic eruptions and release of fine ash.
2. The total eruption volume of Episode 4 was $132 \times 10^6 \text{ m}^3$, which was about the same as that of Episode 1. The average effusion rate over the entire period (eruption rate) was $0.51 \times 10^6 \text{ m}^3 \text{ day}^{-1}$ ($5.9 \text{ m}^3 \text{ s}^{-1}$), which was two to three times higher than that in Episode 1 ($0.20 \times 10^6 \text{ m}^3 \text{ day}^{-1}$: $2.3 \text{ m}^3 \text{ s}^{-1}$).
3. In Stage 1, most of the lava effused from the NE vent and covered the northern half of the island. The average effusion rate was about $0.46 \times 10^6 \text{ m}^3 \text{ day}^{-1}$ ($5.3 \text{ m}^3 \text{ s}^{-1}$). The activity was basically similar to that of Episodes 1–3 in terms of the prevalence of effusive activity, and pyroclastic rocks accounted for about 1–15% of the erupted volume. However, the high effusion rate resulted in a topographic difference, specifically the prevalence of long, broad lava flows.
4. In stage 2, an intensive lava-fountain activity occurred with a high effusion rate, and the pyroclastic cone grew rapidly. The maximum effusion rate was five times higher ($2.6 \times 10^6 \text{ m}^3 \text{ day}^{-1}$: $30 \text{ m}^3 \text{ s}^{-1}$) than the eruption rate of Episode 4. Pyroclastic rocks accounted for 45–88% of the entire erupted volume. Lava flows with rafted cone material were generated due to partial collapse of the pyroclastic cone, and those possibly caused by intensive spatter falls on the slope were also formed. These were distributed over the southern half of the island.
5. In Stage 3, there was almost no growth of the pyroclastic cone, and only fine ash was released due to the continuous phreatomagmatic eruptions.
6. Among the series of activities of Nishinoshima since 2013, the behavior of Episode 4 deviated significantly from a trend of continuous diminishing activity from Episode 1 to Episode 3. Further, in contrast to the previous Episode 1–3 activities, the mode of activity changed abruptly from effusive to intensive lava fountaining to finally continuous phreatomagmatic.

7. Characteristics observed in the Episode 4 activity can be explained by a model in which volatile-rich magma was supplied from the deeper part to the magma chamber prior to the Episode 4 activity. When the volatile-rich magma reached the shallow part of the conduit in Stage 2, fragmentation occurred due to rapid volume expansion, which ejected large amounts magma and formed the intensive lava fountain.
8. A rapid increase in SO₂ emission was observed in synchrony with the occurrence of the intensive lava fountain in Stage 2. This confirms that volatile-rich magma had started to erupt at this time.
9. The ash fragments from Stage 2 have an undifferentiated composition (SiO₂ 54–55 wt%) compared to the lava from Episodes 1–3 (SiO₂ 59–60 wt%), which could be the volatile-rich magma supplied from the deeper part of the magma conduit system.
10. Beginning with the late period of Stage 1, large-scale discolored-seawater areas began to appear. The discolored-seawater areas are thought to have resulted from mixing of seawater with the hydrothermal water released from the subaqueous parts of the edifice, and this hydrothermal venting was associated with the ascent of volatile-rich magma to a shallow depth.

Abbreviations

ALOS-2: Advanced Land Observing Satellite 2; DEM: Digital Elevation Model; DRE: Dense rock equivalent; GCOM-C: Global Change Observation Mission-Climate; JAXA: Japan Aerospace Exploration Agency; JMA: Japan Meteorological Agency; MODTRAN: MODerate resolution atmospheric TRANsmission; NASA: National Aeronautics and Space Administration; NICT: National Institute of Information and Communications Technology; OMPS: Ozone Mapping and Profiler Suite; PALSAR-2: Phased Array type L-band Synthetic Aperture Radar-2; R1.6Mx: Spectral radiance of the pixel showing the maximum value in the heat source area in 1.6-μm band images; SAR: Synthetic aperture radar; SGLI: Second-Generation Global Imager; TROPOMI: Tropospheric Monitoring Instrument Images; TSM: Total suspended matter.

Acknowledgements

The ALOS-2 images were provided by JAXA/EORC. The Himawari-8 AHI data used in this study were received by the Meteorological Research Center of the Japan Meteorological Agency and processed and managed by K. Murata of NICT. We thank N. Hokanishi of the Earthquake Research Institute, University of Tokyo, for the chemical analysis. We also thank the Japan Coast Guard and Japan Meteorological Agency for the use of some of their photographs in this paper. The rock samples of Stage 2 were offered by the Japan Meteorological Agency. Comments from M. Yasui of Nihon University and an anonymous reviewer were significantly helpful for improving the manuscript.

Authors' contributions

Conceptualization and methodology, TK; software, AY; chemical analysis, AY; writing—original draft preparation, TK; writing—review and editing, FM and MI; supervision, TO, SN, KN, YH and HM. All authors have read and agreed to the published version of the manuscript.

Funding

This work was supported by a Grant-in-Aid for Scientific Research from the Japan Society for the Promotion of Science, Kakenhi C (Grant No. 19K04011 to TK); Second Research Announcement on the Earth Observations (PI No. ER2GCF111 to TK) from the JAXA Earth Observation Research Center (JAXA/EORC); Earthquake and Volcano Hazards Observation and Research Program of the Ministry of Education, Culture, Sports, Science and Technology of Japan (No. ERI 07); and Cross-ministerial Strategic Innovation Promotion Program II (Enhancement of Societal Resiliency against Natural Disasters).

Availability of data and materials

This paper is based on published data that are identified in the references. The Himawari-8 images used in this study are available from the Himawari project website, <https://sc-web.nict.go.jp/himawari/himawari-archive.html>, developed by the NICT Science Cloud.

Declarations

Ethics approval and consent participate

Not applicable.

Competing interests

The authors declare that they have no competing interests.

Author details

¹Earthquake Research Institute, The University of Tokyo, 1-1-1 Yayoi, Bunkyo-ku, Tokyo 113-0032, Japan. ²Volcanic Fluid Research Center, Tokyo Institute of Technology, 641-36 Kusatsu, Agatsuma, Gunma 377-1711, Japan. ³National Research Institute for Earth Science and Disaster Resilience, 3-1 Tennodai, Tsukuba-shi, Ibaraki 305-0006, Japan. ⁴Center for Environmental Remote Sensing, Chiba University, 1-33 Yayoi-cho, Inage-ku, Chiba-shi, Chiba 263-8522, Japan. ⁵Japan Aerospace Exploration Agency (JAXA), Earth Observation Research Center, 2-1-1 Sengen, Tsukuba, Ibaraki 305-8505, Japan.

Received: 29 August 2021 Accepted: 11 January 2022

Published online: 21 February 2022

References

- Alidibirov M, Dingwell D (1996) Magma fragmentation by rapid decompression. *Nature* 380:146–148. <https://doi.org/10.1038/380146a0>
- Berk A, Bernstein LS, Robertson DC (1989) MODTRAN: a moderate resolution model for LOWTRAN 7. Tech Rep, GL-TR-89-0122, Geophys Lab, AFSC, Hanscom AFB, MA. <https://apps.dtic.mil/dtic/tr/fulltext/u2/a214337.pdf>. Accessed 3 Sept 2020
- Calvari S, Neri M, Pinkerton H (2003) Effusion rate estimations during the 1999 summit eruption on Mount Etna, and growth of two distinct lava flow fields. *J Volcanol Getherm Res* 119:107–123. [https://doi.org/10.1016/S0377-0273\(02\)00308-6](https://doi.org/10.1016/S0377-0273(02)00308-6)
- Coppola D, Laiolo M, Piscopo D, Cigolini C (2013) Rheological control on the radiant density of active lava flows and domes. *J Volcanol Getherm Res* 249:39–48. <https://doi.org/10.1016/j.jvolgeores.2012.09.005>
- Coppola D, Barsotti S, Cigolini C, Laiolo M, Pfeffer MA, Ripepe M (2019) Monitoring the time-averaged discharge rates, volumes and emplacement style of large lava flows by using MIROVA system: the case of the 2014–2015 eruption at Holuhraun (Iceland). *Ann Geophys* 62:VO221. <https://doi.org/10.4401/ag-7749>
- Geospatial Information Authority of Japan (2018) Latest observation results on Nishinoshima (as of January 2018). <https://www.gsi.go.jp/kanri/kanri41009.html> (in Japanese). Accessed 11 June 2021.
- Geospatial Information Authority of Japan (2021) Topographic map, NG-54-20-1-2 Nishinoshima, <https://maps.gsi.go.jp/#16/27.244719/140.881430/&base=std&ls=std&disp=1&vs=c1j0h0k0l0u0t0z0r0s0m0f1>. Accessed 11 June 2021
- Gonnermann HM, Manga M (2007) The fluid mechanics inside a volcano. *Annu Rev Fluid Mech* 39:321–356. <https://doi.org/10.1146/annurev.fluid.39.050905.110207>
- Gonnermann HM, Manga M (2012) Dynamics of magma ascent in the volcanic conduit. In: Fagents SA, Gregg TKP, and Lopes RMC (eds) Modeling

- volcanic processes: the physics and mathematics of volcanism. Cambridge University Press, Cambridge, pp 55–84. <https://doi.org/10.1017/CBO9781139021562.004>
- Guest JE, Kilburn CRJ, Pinkerton H, Duncan AM (1987) The evolution of lava flow-fields: observations of the 1981 and 1983 eruptions of Mount Etna, Sicily. *Bull Volcanol* 49:527–540. <https://doi.org/10.1007/BF01080447>
- Harris AJL (2013) Thermal remote sensing of active volcanoes, a user's manual. Cambridge University Press, Cambridge
- Harris AJL, Baloga SM (2009) Lava discharge rates from satellite-measured heat flux. *J Geophys Res* 36:19302 (1–5). <https://doi.org/10.1029/2009GL039717>
- Harris AJL, Blake S, Rothery DA, Stevens NF (1997) A chronology of the 1991 to 1993 Mount Etna eruption using advanced very high resolution radiometer data: implications for real-time thermal volcano monitoring. *J Geophys Lett* 102:7985–8003. <https://doi.org/10.1029/96JB03388>
- Harris AJL, Dehn J, Calvari S (2007) Lava effusion rate definition and measurement: a review. *Bull Volcanol* 70:1–22. <https://doi.org/10.1007/s00445-007-0120-y>
- Houghton BF, Gonnermann HM (2008) Basaltic explosive volcanism: constraints from deposits and models. *Chem Erde* 68:117–140
- Japan Aerospace Exploration Agency (2021a) ALOS Research and Application Project. https://www.eorc.jaxa.jp/ALOS/a/en/index_e.htm. Accessed 21 June 2021
- Japan Aerospace Exploration Agency (2021b) JASMES SGLI Near-Realtime Monitor. https://www.eorc.jaxa.jp/cgi-bin/jasmes/sgli_nrt/index.cgi?lang=en. Accessed 21 June 2021
- Japan Coast Guard (2017) Bathymetric Chart: No 6556⁸ NISHI-NO-SHIMA
- Japan Coast Guard (2021) Nishinoshima. <https://www1.kaiho.mlit.go.jp/GJJUT/SUKOKUSA/kaiikiDB/kaiyo18-e1.htm>. Accessed 11 June 2021
- Japan Meteorological Agency (2021) Himawari-8/9 operational information. <http://www.data.jma.go.jp/mscweb/en/operation8/>. Accessed 21 June 2021
- Kaneko T, Takasaki K, Maeno F, Wooster MJ, Yasuda A (2018a) Himawari-8 infrared observations of the June–August 2015 Mt Raung eruption, Indonesia. *Earth Planet Space* 70:89. <https://doi.org/10.1186/s40623-018-0858-9>
- Kaneko T, Yasuda A, Yoshizaki Y, Takasaki K, Honda Y (2018b) Pseudo-thermal anomalies in the shortwave infrared bands of the Himawari-8 AHI and their correction for volcano thermal observation. *Earth Planet Space* 70:175. <https://doi.org/10.1186/s40623-018-0946-x>
- Kaneko T, Maeno F, Yasuda A (2019a) Observation of the eruption sequence and formation process of a temporary lava lake during the June–August 2015 Mt. Raung eruption, Indonesia, using high-resolution and high-frequency satellite image datasets. *J Volcanol Geotherm Res* 377:17–32. <https://doi.org/10.1016/j.jvolgeores.2019.03.016>
- Kaneko T, Maeno F, Yasuda A, Takeo M, Takasaki K (2019b) The 2017 Nishinoshima eruption: combined analysis using Himawari-8 and multiple high-resolution satellite images. *Earth Planet Space* 71:140. <https://doi.org/10.1186/s40623-019-1121-8>
- Kaneko T, Yasuda A, Fujii T (2021) Simple empirical method for estimating lava-effusion rate using nighttime Himawari-8 1.6- μ m infrared images. *Earth Planet Space* 73:37. <https://doi.org/10.1186/s40623-021-01372-w>
- Kazahaya K, Shinohara H, Uto K, Odai M, Nakahori Y, Mori H, Iino H, Miyashita M, Hirabayashi J (2004) Gigantic SO₂ emission from Miyakejima volcano, Japan, caused by caldera collapse. *Geology* 32:425–428. <https://doi.org/10.1130/G20399.1>
- Kilburn CRJ (2000) Lava flows and flow fields. In: Sigurdsson H (ed) *Encyclopedia of volcanoes*. Academic Press, San Diego, CA, pp 291–306
- La Spina G, Arzilli F, Llewellyn EW, Burton MR, Clarke AB, de' Michieli Vitturi M, Polacci M, Hartley ME, Di Genova D, Mader HM (2021) Explosivity of basaltic lava fountains is controlled by magma rheology, ascent rate and outgassing. *Earth Planet Sci Lett* 553:116658. <https://doi.org/10.1016/j.epsl.2020.116658>
- Macdonald GA (1972) *Volcanoes*. Prentice-Hall, Englewood Cliff, New Jersey
- Maeno F, Nakada S, Kaneko T (2016) Morphological evolution of a new volcanic islet sustained by compound lava flows. *Geology* 44(4):259–262. <https://doi.org/10.1130/G37461.1>
- Maeno F, Nakano S, Yoshimoto M, Ohminato T, Watanabe A, Kawakami K, Chida T, Takeo M (2017) First Landing and Survey of a New Volcanic Island: Nishinoshima. *J Geogr* 126(1): N1–13. (in Japanese) <http://journal.geog.or.jp/images/articles/126-1/N1.pdf>. Accessed 11 June 2021
- Maeno F, Yasuda A, Nakano S, Yoshimoto M, Ohminato T, Watanabe A, Kaneko T, Nakada S, Takeo M (2018) Formation process of a new volcanic island at Nishinoshima, Ogasawara, Japan, inferred from eruptive products. *J Adv Mari Sci Tech Soc* 24:35–44. (in Japanese with English abstract)
- McGetchin TR, Settle M, Chouet BA (1974) Cinder cone growth modeled after Northeast Crater, Mount Etna, Sicily. *J Geophys Res* 79:3257–3272. <https://doi.org/10.1029/JB079i023p03257>
- NASA Goddard Space Flight Center (2021) Global Sulfur Dioxide Monitoring Home Page. <https://so2.gsfc.nasa.gov/>. Accessed 21 June 2021
- NICT Science cloud (2021) Himawari-8 Realtime web. <https://sc-web.nict.go.jp/himawari/>. Accessed 21 June 2021
- Ossaka J, Adachi N, Tsuchide M, Nogami K (2000) Chemical compositions of discolored sea water around Izu-Oshima at the 1986 eruption. *Bull Vol Soc Japan* 45:271–280. (in Japanese with English abstract)
- Pioli L, Erlund E, Johnson E, Cashman K, Wallace P, Rosi M, Granados HD (2008) Explosive dynamics of violent Strombolian eruptions: the eruption of Parícutin Volcano 1943–1952 (Mexico). *Earth Planet Sci Lett* 271:359–368. <https://doi.org/10.1016/j.epsl.2008.04.026>
- Pyle DM, Pyle DL (1995) Bubble migration and the initiation of volcanic eruptions. *J Volcanol Geotherm Res* 67:227–232. [https://doi.org/10.1016/0377-0273\(94\)00111-5](https://doi.org/10.1016/0377-0273(94)00111-5)
- Schmincke H-U (2004) *Volcanism*. Springer, Berlin
- Sides IR, Edmonds M, MacLennan J, Swanson DA, Houghton BF (2014) Eruption style at Kilauea Volcano in Hawai'i linked to primary melt composition. *Nat Geosci* 7:464–469
- Sparks RSJ (1978) The dynamics of bubble formation and growth in magmas: a review and analysis. *J Volcanol Geotherm Res* 3:1–37. [https://doi.org/10.1016/0377-0273\(78\)90002-1](https://doi.org/10.1016/0377-0273(78)90002-1)
- Stern RJ, Fouch MJ, Klemperer SL (2004) An overview of the Izu-Bonin-Mariana Subduction Factory. In: Eiler J (ed) *Geophysical monograph Series* 138. American Geophysical Union, pp 175–222
- Sumner J (1998) Formation of clastogenic lava flows during fissure eruption and scoria cone collapse: the 1986 eruption of Izu-Oshima Volcano, eastern Japan. *Bull Volcanol* 60:195–212. <https://doi.org/10.1007/s004450050227>
- Toratan M (2021) SGLI Algorithm Theoretical Basis Document: Total suspended matter concentration (Version 2 Rev.1). https://suzaku.eorc.jaxa.jp/GCOM_C/data/ATBD/ver2/V2ATBD_O3AB_TSM_Toratan_r1.pdf. Accessed 21 July 2021
- Umino S, Nakano S (2007) *Geology of the Chichijima Retto District. Quadrangle Series, 1:50,000*. Geological Survey of Japan, AIST, p 71 (in Japanese with English abstract)
- Wadge G (1981) The variation of magma discharge during basaltic eruption. *J Volcanol Geotherm Res* 11:139–168. [https://doi.org/10.1016/0377-0273\(81\)90020-2](https://doi.org/10.1016/0377-0273(81)90020-2)
- Walter LS, Salisbury JW (1989) Spectral characterization of igneous rocks in the 8- to 12- μ m region. *J Geophys Res* 94:9203–9213. <https://doi.org/10.1029/JB094iB07p09203>
- Wolfe EW, Neal CA, Banks NG, Duggan TJ (1988) Geologic observations and chronology of eruptive events. In: Wolfe EW (ed) *The Puu Oo Eruption of Kilauea Volcano, Hawaii: Episodes 1 through 20, January 3, 1983, through June 8, 1984*. USGS Prof Pap 1463: 1–97
- Woods AW, Cardoso SSS (1997) Triggering basaltic volcanic eruptions by bubble-melt separation. *Nature* 385:518–520
- Wright R, Blake S, Harris AJL, Rothery DA (2001) A simple explanation for the space-based calculation of lava eruption rates. *Earth Planet Sci Lett* 192:223–233. [https://doi.org/10.1016/S0012-821X\(01\)00443-5](https://doi.org/10.1016/S0012-821X(01)00443-5)
- Yanagisawa H, Iino H, Ando S, Takagi A, Oikawa T (2020) Violent Strombolian Eruption from June to August 2020 of Nishinoshima Island, Ogasawara Islands, Japan. *Bull Vol Soc Japan* 65:119–124. (in Japanese)

Publisher's Note

Springer Nature remains neutral with regard to jurisdictional claims in published maps and institutional affiliations.